



EFFECT OF STRAIN RATE ON PLASTIC FLOW AND FAILURE IN POLYCRYSTALLINE TUNGSTEN

T. DÜMMER¹, J. C. LASALVIA², G. RAVICHANDRAN³ and M. A. MEYERS^{4†}

¹Department of Mechanical Engineering, Universität Karlsruhe (TH), Karlsruhe, Germany, ²Materials Division, Army Research Laboratory, Aberdeen Proving Ground, Aberdeen, Maryland 21005, U.S.A., ³Graduate Aeronautical Laboratories, California Institute of Technology, Pasadena, California, U.S.A. and ⁴Department of Applied Mechanics and Engineering Sciences, University of California, San Diego, La Jolla, CA 92093, U.S.A.

(Received 27 August 1996; accepted 22 June 1998)

Abstract—Polycrystalline tungsten (less than 100 p.p.m. impurities) was subjected to different heat treatments to yield different grain morphologies and tested at quasi-static (3×10^{-3}) and dynamic (10^3 – 4×10^3 /s) strain rates. Three mechanisms of deformation were identified and evaluated: slip, twinning, and intergranular cracking. Whereas plastic flow by slip has considerable strain-rate sensitivity in tungsten (which is found to be well represented by the Mechanical Threshold Stress constitutive equation) the cohesive strength of the grain boundaries was found to decrease with heat treatment temperature, but was insensitive to strain-rate changes. Low-strain-rate deformation yielded limited damage at strains as high as 0.25, whereas high-strain-rate deformation led to catastrophic failure at strains between 0.05 and 0.10. Slip and grain-boundary decohesion being competing deformation mechanisms, the material undergoes a ductile-to-brittle transition as the strain rate is increased from 10^{-3} to 10^3 /s. Two failure modes are identified: debonding initiated by shear along a grain-boundary facet (similar to the wing-crack mechanism) and debonding initiated at voids. The interactions between microcracks and twins are characterized, and there is both evidence of fracture initiation at twins (intergranular cracks), and twin initiation at cracks (transgranular cracks). Calculations based on existing wing-crack models enable the estimation of the grain-boundary cohesive energies. © 1998 Acta Metallurgica Inc. Published by Elsevier Science Ltd. All rights reserved.

1. INTRODUCTION

Refractory metals such as tungsten (W) and its alloys are finding increasing structural applications which involve impact loading [1–3]. The high density ($\rho = 19.3$), high strength, good ductility, and high melting point makes tungsten an attractive candidate material in such applications. One such application involves kinetic energy penetrators which are long rods fired from smooth bore, large caliber guns in tanks; muzzle velocities above 1000 m/s are achieved, and rolled homogeneous armor thicknesses exceeding 1 m can be pierced. The massive clean-up effort after Desert Storm revealed the major problem with the past generation of kinetic energy penetrators: they were made of depleted uranium which has the desired density ($\rho = 19.05$) and ductility, but is pyrophoric and highly toxic after impact. A new generation of kinetic energy penetrators utilizing tungsten alloys which have an equally high density is being considered. The mechanical properties of the material at high strain rates is of great importance in the design and analysis of such applications. Although the principal (non-uranium) technological materials

developed for a penetrator are W-based composites, in which the continuous phase is a Ni–Fe, Ni–Co or other alloy, it is important to fully understand the strain-rate dependent response of pure tungsten.

Tungsten undergoes a ductile-to-brittle transition. The transition temperature (DBTT) increases when the strain rate is increased, leading to fracture with little or no macroscopic plastic deformation below DBTT [4]. Lassila and Gray [5] reported a ductile-to-brittle transition in W as the temperature is reduced from 400 to 22°C. Ravichandran [6] and Subhash *et al.* [7, 8] obtained such a transition when the strain rate is increased from 10^{-3} to 10^3 /s. Chiem and Shyan [9] have carried out similar experiments. In addition to slip, twinning and grain-boundary decohesion can play major roles during deformation. The objective of the present investigation is to study and quantify the micromechanisms responsible for the ductile-to-brittle transition undergone by polycrystalline tungsten, when deformed in compression under a wide range of strain rates.

2. EXPERIMENTAL PROCEDURES

The as-received material consists of powder metallurgical, hot sintered, polycrystalline tungsten. It

†To whom all correspondence should be addressed.

Table 1. Average chemical composition of the tungsten used in the present study

Impurity	Fe	Mo	Ni	K	Na	C	O	N
Content (p.p.m.)	4	18	2	<10	<5	29	<10	<10

was obtained from Sylvania GTE Products Corporation in the form of cylindrical bars with a diameter of 25.4 mm. Tungsten powder was pressed at a temperature of 1200°C, then sintered at 2600°C for 1 h by self-resistance heating in a hydrogen atmosphere. The particle size of the powder was approximately 4 μm . The sintered rods of 1 inch diameter were then rolled at 1200°C to the final diameter of 6.35 mm. The average chemical composition of the material as determined by the manufacturer is given in Table 1. It is considered high purity tungsten, with a total impurity content of less than 0.01%.

In order to obtain different grain morphologies, the as-received tungsten was subjected to three different heat treatments. All the material was annealed in a vacuum furnace at 1750°C for 15 h in order to recrystallize the textured microstructure produced by the rolling process. In order to obtain three different grain sizes, portions of the tungsten rods were further heat treated at 2600°C for 3.5 h and portions at 2800°C for 3.5 h. The heat treatments were conducted in an ultra-pure dry argon atmosphere (impurities in p.p.m.: H₂O, 3; N₂, 6; O₂, 2; THC, 1) to prevent both oxidation and hydrogen embrittlement.

After heat treatment, the tungsten rods [6.35 mm diameter (D)] were cut into cylindrical specimens for mechanical testing. The quasi-static testing was conducted using a servo-hydraulic material testing system and the high-strain-rate testing was done using a split Hopkinson (Kolsky) pressure bar system. The specimens for quasi-static testing were cut to a length of $L = 6.35$ mm ($L/D \sim 1$). The specimens for dynamic split Hopkinson bar compression tests were cut to a length of $L = 3.68$ mm in accordance with the recommended ratio $L/D \sim 0.5$ [10]. Finally, the faces of the cylinders were ground flat and parallel. The split Hopkinson bar experiments were carried out at strain rates of 10^3 , 3×10^3 , and $4 \times 10^3/\text{s}$. The bars in the split Hopkinson bar set-up were made of maraging steel 12.5 mm in diameter. The details of split Hopkinson pressure bar testing of metals can be found in Follansbee [10].

In order to prevent indentation of the specimen into the bar interfaces, tungsten-carbide (WC) platens were placed between each specimen-bar interface. It is necessary to match the acoustic impedances (ρcA) of the bar material and that of the platens so as to minimize spurious reflections at the interfaces which will affect the reflected and transmitted signals. Due to the difference in acoustic impedance of the bar material (steel) and platens

(WC), the diameter of the platens was dictated by the impedance equilibrium

$$A_1 \rho_1 c_1 = A_2 \rho_2 c_2 \quad (1)$$

where A_1 , A_2 , ρ_1 , ρ_2 , c_1 , and c_2 are the cross-sectional areas, densities, and longitudinal bar wave speeds, respectively, for the bar and the platen material. The impedance matching yields a WC platen diameter of 8.4 mm for a bar diameter of 12.5 mm for maraging steel. The use of platens to minimize indentation into the bars and pulse distortion has been analyzed in detail by Chen *et al.* [11].

The pulses in a split Hopkinson bar contain oscillations (Pochhammer–Chree) due to geometric dispersion of wave propagation in the bars. To minimize the high frequency components in the input pulse, copper cushions were placed at the interface between the incident bar and the striker bar. This yields a stress pulse which is relatively free of oscillations within the incident bar after impact of the striker. By adjusting the diameter and thickness of the cushion, it is possible to achieve reflected signals of constant amplitude. Thus a “constant” strain rate during deformation can be achieved. Further details of this technique are given by Nemat-Nasser *et al.* [12]. To limit the extent of deformation of the specimen, a stopper ring was used. The stopper ring is made of a high strength steel alloy. The stopper ring has a much larger outer diameter than the specimen and the length is smaller than the specimen and is placed concentrically over the specimen. The inner diameter is chosen such that no contact between the specimen and the ring takes place during deformation. When the specimen is initially subjected to deformation, the stopper ring does not carry any load but when the specimen is deformed to the same length as the stopper ring, the ring also carries load. In the case of high-strain-rate deformation, the amplitude of the incident pulse is chosen such that the specimen does not undergo further deformation once the ring begins to carry load. Under quasi-static loading, with displacement control, a sudden increase in load due to the contact with stopper rings can be used to terminate the deformation of the sample. The difference in length between the specimen and the stopper ring determines the maximum strain experienced by the specimen. Further information on the use of stopper rings for high strain rate compression testing are given by Ref. [12]. Strains as small as 0.02 can be achieved using the stopper rings.

The quasi-statically and dynamically tested specimens were characterized by optical and scanning

electron microscopy. The fracture surfaces of the catastrophically failed samples were further investigated via scanning electron microscopy. The polished surfaces were lightly etched using a water solution of 5% $K_3Fe(CN)_6$ and 5% KOH. The samples were swabbed with the etchant for 5–15 s. A quantitative analysis of the damage introduced to the tungsten specimens by mechanical testing was carried out by means of optical microscopy. Six micrographs at a magnification of 100 were taken of the longitudinal section of each sample. Care was taken to align the specimen loading axis parallel to one axis of the micrograph. Only a light etching was applied in order not to alter the crack shape nor to increase the width of the grain boundaries which would make the distinction between grain-boundary debonding and intact grain boundaries difficult. Correct etching and observation enabled distinguishing between grain-boundary cracks and grain boundaries.

3. RESULTS AND DISCUSSION

3.1. Effect of heat treatments on microstructure

The as-received microstructure is shown in Fig. 1(a). In the plane perpendicular to the rolling direction an equiaxed grain structure is evident. The longitudinal planes show a strongly elongated structure in the rolling direction. Body-centered-cubic metals are known to exhibit a (011) crystallographic texture in either the rolling, forging or extrusion direction. The apparent grain diameter, obtained by the linear intercept method and multiplying by 1.5 [13], is equal to 25 μm . Annealing the specimens at 1750, 2600, and 2800°C yielded grain diameters equal to 83.7, 98.4, and 111.0 μm , respectively. Note that the 2600 and 2800°C treatments were preceded by the 1750°C treatment. The elongation of the grains, still present after the 1750°C treatment (intercepts are: $l_x=45.8 \mu\text{m}$; $l_y=43.1 \mu\text{m}$; $l_z=60.4 \mu\text{m}$), essentially disappears after the 2600 and 2800°C treatments. The structure of the material annealed at 2600°C is shown in Fig. 1(b).

3.2. Mechanical characterization

The stress–strain response of the W specimen subjected to the different heat treatments is shown in Fig. 2. The quasi-static curves are solid lines and the dynamic curves are dashed-dotted ($10^3/\text{s}$) and dashed ($4 \times 10^3/\text{s}$) lines. The quasi-static curves of the annealed conditions are very similar; the yield stress is approximately 0.75 GPa and is not a strong function of grain size. The progressive disappearance of the yield phenomenon with increased treatment temperature is caused by impurity segregation to the grain boundaries. “Unlocking” of the dislocations results and causes the more round yield point. The as-received condition exhibits a higher yield stress (~ 1.2 GPa) and a lower work-hardening

rate because it is in a hardened condition, containing a higher dislocation density. The high strain-rate sensitivity of the as-received material is expected; the work-hardening rates at low and high strain rates are similar. This is the classical response for b.c.c. metals, in which the plastic flow is governed by overcoming of the Peierls barriers. Zerilli and Armstrong [14] describe this behavior well; Meyers *et al.* [15] obtained a similar response for tantalum. On the other hand, f.c.c. metals like copper show a strain-rate dependence of work hardening [16]. It should be noted that at high strain rates, the inherent oscillations due to elastic wave dispersion and lack of stress equilibrium at low strains make the determination of yield inaccurate. The yield stress increased from 1.2 to 2 GPa for the as-received material (a 40% increase); this increase was from 0.8 to 1.15 GPa for the heat-treated conditions, a similar fractional increase. Zurek *et al.* [17] tested similar material (tungsten plate) and obtained results that closely match the as-received material in this investigation: low work hardening and a plastic flow plateau that increased from ~ 1.5 GPa at $10^{-3}/\text{s}$ to 2 GPa at $2 \times 10^3/\text{s}$. This material was, according to Zurek *et al.* [17], in a work-hardened condition.

The failure strain at strain rates on the order of $\sim 10^3/\text{s}$ of the heat treated tungsten (at 1750, 2600, and 2800°C) was found to be approximately ~ 0.07 ; this is significantly lower than under quasi-static loading for the corresponding annealing condition. The specimens fragmented at a strain of ~ 0.25 under quasi-static loading.

3.3. Constitutive modeling

The description of the mechanical behavior of tungsten is modeled using the Zerilli–Armstrong (ZA) and the Mechanical Threshold Stress (MTS) constitutive models.

In the ZA model for b.c.c. materials, the dependence of the flow stress σ on strain ϵ , strain rate, and temperature T is given by

$$\sigma = C_0 + C_1 \exp[-C_3 T + C_4 T \ln \dot{\epsilon}] + C_5 \epsilon_p^n. \quad (2)$$

The athermal stress C_0 takes into account the grain size through a Hall–Petch relation, $C_0 = \sigma_0 + kd^{-1/2}$, where σ_0 is the intrinsic athermal stress contribution, k is a strength coefficient and d is the average grain size for the material. C_1 , C_3 , and C_4 take the strain-rate and temperature and C_5 the strain-hardening effects on the flow stress into account. Equation (2) takes into account that b.c.c. metals do not exhibit a strain-rate and temperature dependence of the work hardening and grain-boundary strengthening (both terms are additive).

The MTS model uses the basic ingredients of the thermally activated dislocation model for plastic flow and includes the effect of strain rate. It is based on the dislocation concepts advanced by

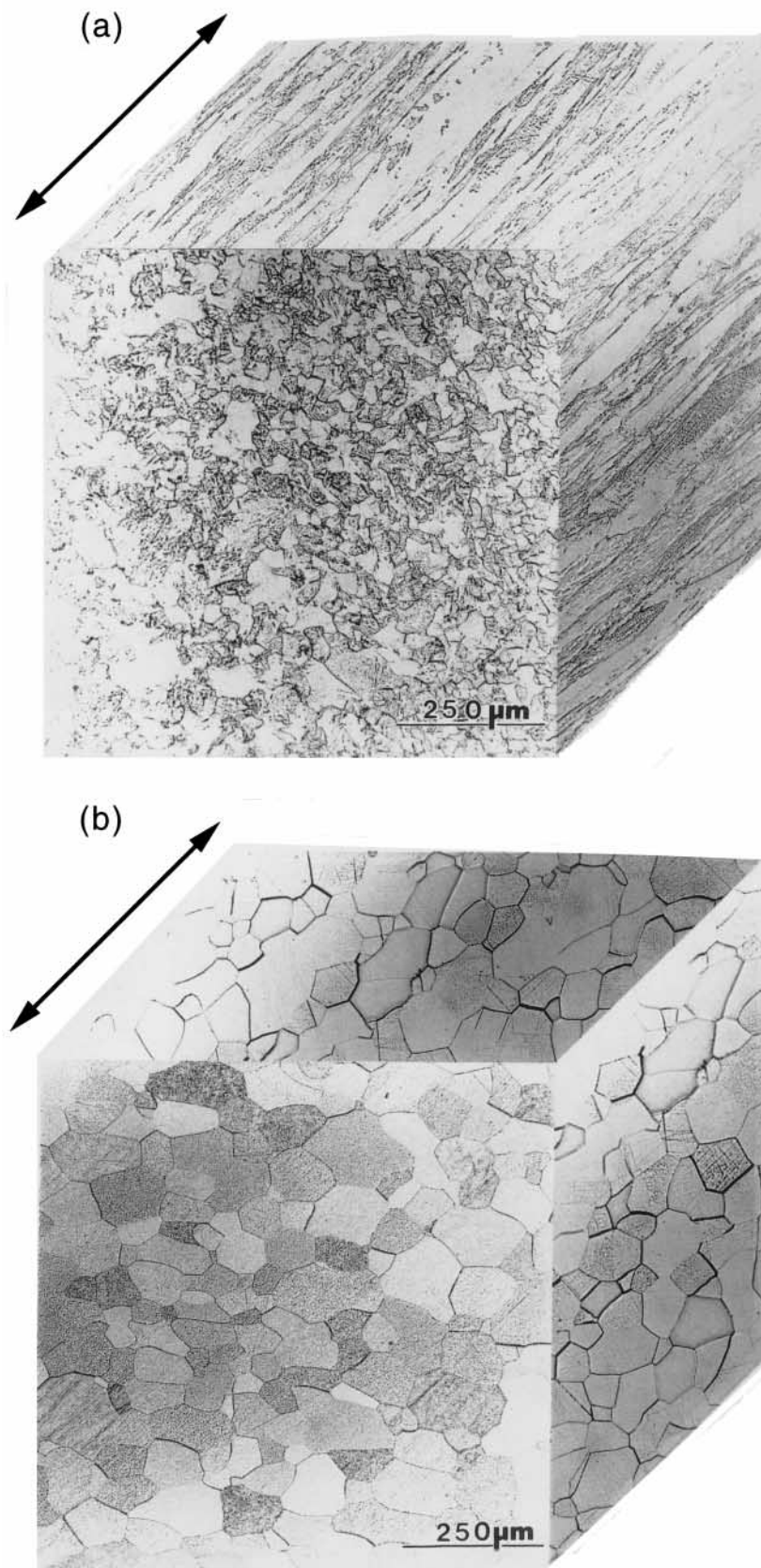


Fig. 1. Longitudinal and transverse sections of: (a) as-received W and (b) W annealed at 2600°C.

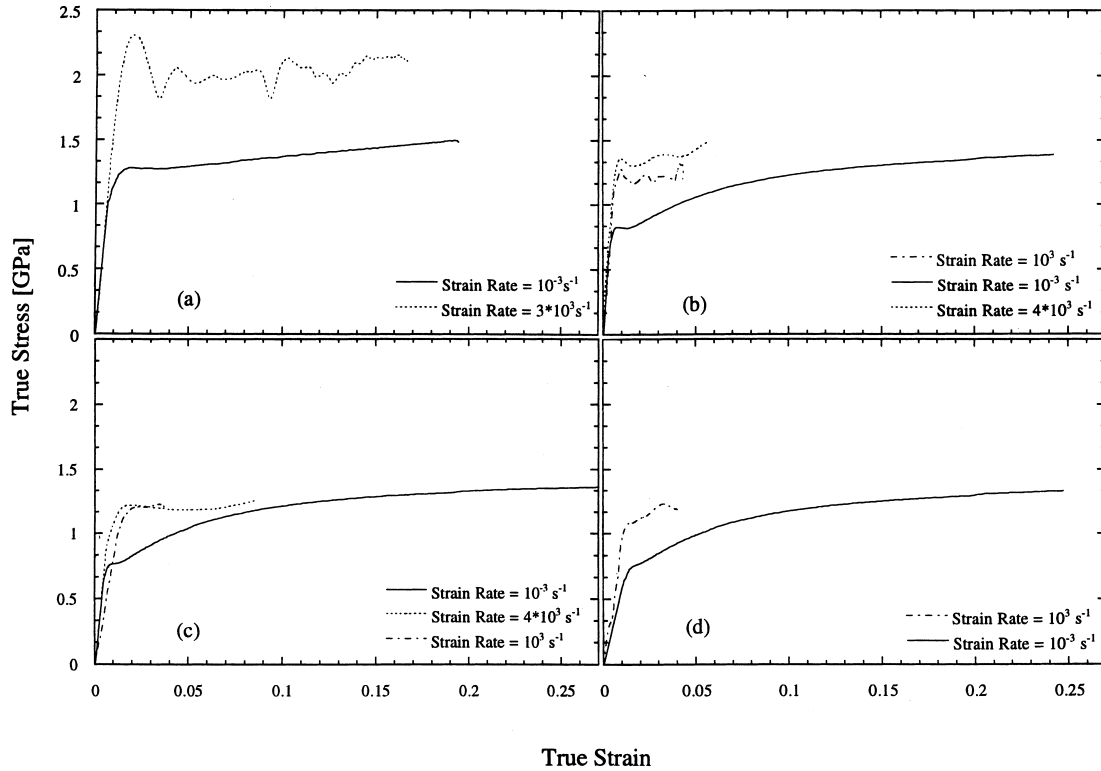


Fig. 2. Stress–strain curves for W at different strain rates: (a) as-received; annealed (b) at 1750°C, (c) at 2600°C, and (d) at 2800°C.

Kocks *et al.* [18] and was originally developed by Follansbee and Kocks [19,20]. The MTS constitutive model can be expressed in the form [21] for stress σ in terms of the athermal (σ_a) and thermal (σ_t) components. For thermally activated glide processes, the relation between the applied stress and the mechanical threshold stress can be expressed as

$$\frac{\sigma_t}{\mu} = \left[1 - \left(\frac{kT}{g_0 \mu b^3} \ln \frac{\dot{\epsilon}_0}{\dot{\epsilon}} \right)^{1/q} \right]^{1/p} \frac{\hat{\sigma}_t}{\mu_0} = S_t(\dot{\epsilon}, T) \frac{\hat{\sigma}_t}{\mu_0} \quad (3)$$

where S_t is a structure factor which is a function of the strain rate and temperature as shown above. The thermal component of the stress consists of two parts, one which is intrinsic (σ_i), and which provides the rate dependence of the flow stress due to intrinsic barriers such as the Peierls stress which does not evolve after yielding and the other, (σ_e), which evolves with strain due to dislocation multiplication, i.e. work hardening. Hence the constitutive law can be rewritten as

$$\frac{\sigma}{\mu} = \frac{\sigma_a}{\mu} + S_t(\dot{\epsilon}, T) \frac{\hat{\sigma}_t}{\mu_0} + S_e(\dot{\epsilon}, T) \frac{\hat{\sigma}_e}{\mu_0} \quad (4)$$

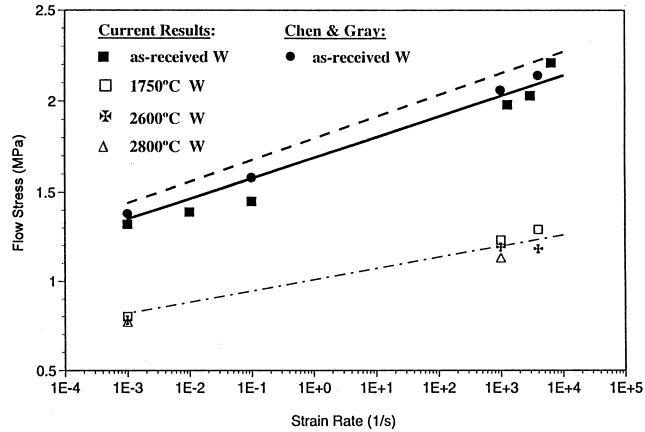
where μ is the temperature dependent shear modulus and μ_0 the shear modulus at a reference temperature. The work hardening is taken into account in the form of a Voce law. The details of the MTS model applied to tungsten can be found in Chen and Gray [21].

The temperature T during high-strain-rate adiabatic deformation is calculated using

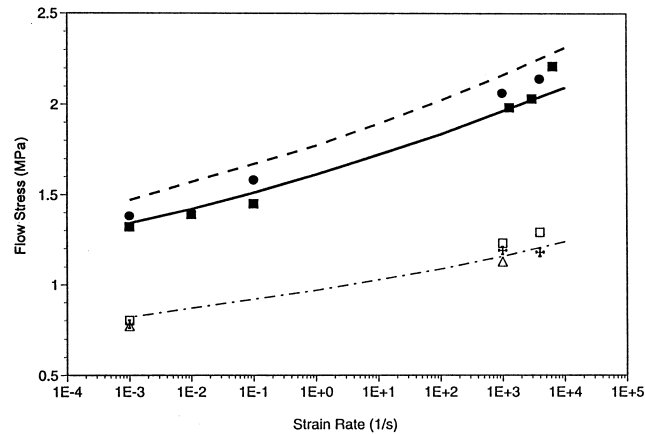
$$T = T_0 + \frac{\beta}{\rho c} \int_0^e \sigma d\zeta \quad (5)$$

where β is the fraction of rate of plastic work converted to heat which is taken to be a constant, 0.9 in our modeling. T_0 is the ambient temperature, and ρ and c are the mass density and the specific heat of the material, respectively.

In Fig. 3(a), the flow stresses at a plastic strain of 0.03, determined from the present mechanical testing, are plotted vs the strain rate and compared with the Zerilli–Armstrong model. The parameter C_1 is chosen in a way that the stress–strain rate curve predicted by equation (2) passes through the data points of the present quasi-static tests for each material condition. Under quasi-static conditions each material yielded by plastic flow as indicated by the stress–strain curves (Fig. 2). In the case of the as-received tungsten the flow stress at a strain rate of $3 \times 10^3/s$ matches closely the one predicted by the ZA model. This indicates that the parameters obtained by Chen and Gray [21] are applicable to the present material and that under dynamic conditions the as-received tungsten yielded by plastic flow. The flow stress of the heat-treated condition is approximately 0.8 GPa at low strain rates. The parameter C_1 was modified for the annealed conditions



(a)



(b)

Fig. 3. Comparison between the observed flow stress dependence on stress rate and constitutive description by (a) the Zerilli–Armstrong model and (b) the MTS model; parameters from Chen and Gray [21].

and a good fit was obtained. The ZA model parameters for the as-received and the annealed (1750, 2600, and 2800°C) tungsten, are given in Table 2. At high strain rates, the heat-treated tungsten at all annealing conditions (1750, 2600, and 2800°C) ex-

hibits flow stresses at a strain of 0.03 well represented by the ZA constitutive description.

It should be pointed out that, when another rationale was used to implement the ZA model, a very poor fit was obtained. This second approach

Table 2. Parameters for the Zerilli–Armstrong (ZA) and MTS models

C_0 (MPa)		C_1 (MPa)		C_3 (/K)		C_4 (/K)		C_5 (MPa)		n
0		†		0.002		0.0001		800		0.6
μ_0 (GPa)	D (GPa)	T_0 (K)	k/b^3 (MPa/K)	σ_a (MPa)	σ_i (MPa)	E_{0i} (/s)	g_{0i}	q_i	p_i	
159.5	33.69	1217	0.671	100	‡	10^8	0.142 8	3/2	1/2	
ϵ_{0e} (/s)	g_{0e}	q_e	p_e	θ_0 (MPa)	α	g_{0es}	σ_{es0} (MPa)	ϵ_{0es} (/s)		
10^7	1.6	1.0	2/3	3000	1	1.775	1035	10^7		

†3000 MPa (Chen and Gray), 2800 MPa (as-received), 1600 MPa (annealed). Parameters for the mechanical threshold stress (MTS) model.‡3230.2 MPa (Chen and Gray), 2900 MPa (as-received), 1600 MPa (annealed).

uses the physically correct assumption that the as-received material is severely work hardened and that, additionally, there are differences in grain size. Both work hardening and grain-size differences can be incorporated into the ZA equation through the parameters C_0 and C_5 , respectively. Body-centered-cubic metals do not exhibit a strain-rate and temperature dependence of the work hardening and grain-boundary strengthening [both terms are additive in equation (2)]. The grain-size parameter C_0 and work-hardening parameters C_5 and n were chosen such that the stress–strain rate curve predicted by equation (2) passes through the data points of the present quasi-static tests for each material condition. In the case of the as-received tungsten the flow stress at a strain rate of $3 \times 10^3/s$ matched exactly that predicted by the ZA model at both low and high strain rates, in accordance with Chen and Gray [21]. The 0.5% flow stress of the annealed conditions is approximately 0.8 GPa at low strain rates. As mentioned, the strain-rate dependence of the flow stress is not sensitive to grain size and dislocation density; this is equivalent to shifting the curve of the predicted stress downwards retaining the other ZA parameters. At high strain rates annealed conditions exhibited a 0.5% flow stress lower than that predicted by the ZA constitutive description. This indicates very clearly that yielding at high strain rates of the three annealed conditions is not well represented by the ZA equation under these assumptions.

The comparison of the experimental results with the MTS model is shown in Fig. 3(b). For the as-received tungsten, the parameters of Chen and Gray [21] were used, with only a minor adjustment in σ_i (from 3230 to 2900 MPa) to take into account the slightly lower yield stress observed in the current experiments. For the annealed conditions, σ_i was reduced to 1600 MPa to obtain a fit at $10^{-3}/s$. All other parameters by Chen and Gray [21] were retained and are shown in Table 2. The fit is found to be excellent both for the as-received and annealed conditions.

The results shown in Fig. 3 show very clearly that both the ZA and MTS models represent the overall response of the tungsten satisfactorily, and that the onset of inelastic deformation can be attributed to dislocation activity for all, as-received and annealed, conditions.

3.4. Characterization of damage

We classify damage into microcrack and macrocrack damage. Microcracks have a scale on the order of the grain size, and macrocracks of the specimen size. The most obvious feature concerning damage in the heat-treated materials is that it is governed predominantly by grain-boundary decohesion. Figure 4 gives an example of the appearance of damage within the heat-treated material when subjected to high strain rates. Longitudinal and

cross sections of a specimen annealed at 2600°C and deformed to a strain of 0.05 at a strain rate of $10^3/s$ are shown. Damage by macrocracks (marked by arrows 1) parallel to the loading direction is clear. This failure mode is commonly referred to as axial splitting [22, 23]. The dark dots (arrow 2) represent grains that were pulled out during polishing. They had been separated by debonded interfaces. Note that the specimen shown in Fig. 4 did not fail. The transverse section shows, Fig. 4(a), that macrocracks form radially, starting at the specimen perimeter and propagate towards the center. The center of this section exhibits numerous linked microcracks with no favored orientation.

Figure 5 shows representative areas from longitudinal sections for the materials annealed at 1750 and 2600°C and deformed quasi-statically to a strain of approximately 0.25 (loading direction is top to bottom). The 1750°C annealed material, Fig. 5(a), exhibits a preferred orientation in grain-boundary debonding (microcracks are indicated by arrows), corresponding to the axially textured microstructure. In the equiaxed 2600°C annealed condition, Fig. 5(b), the debonding appears to be less oriented.

The amount of damage accumulated within the specimens tested dynamically is much higher than for the ones deformed quasi-statically, at the same plastic strain. For the quasi-statically tested specimens, the shape of the stress–strain curves and the presence of low damage after straining above 0.20 indicates a typical ductile process, as shown by Bilello [24]. Figure 6 shows the as-received W after dynamic testing; a mixture of intergranular and transgranular (arrows) fracture characterizes the as-received material. In quasi-static testing, the as-received material did not exhibit microcrack damage up to a strain of 0.20. The 2600°C annealed specimen deformed to a strain of 0.052 at a strain rate of $4 \times 10^3/s$ as shown in Fig. 6(b); mainly intergranular cracks characterize the annealed material. An axial macrocrack is indicated by arrow 1. The right-hand side of the image shows misaligned microcracks which are frequently related to twin-grain-boundary intersections (arrows 2). Optical microscopy at higher magnification reveals that beside grain-boundary failure, twin formation is associated with transgranular fracture.

The Appendix A provides a quantitative analysis of crack orientation and density for the various conditions and strain rates. These results show in a clear fashion that (a) the damage by micro- and macrocracking increases with increasing strain and strain rate and (b) that the angular distribution of cracks is initially random (microcracks) and becomes progressively more aligned with the loading axis as the cracks grow or coalesce (macrocracks).

Figure 7(a) (from W annealed at 2600°C and tested at $10^3/s$) shows a twin intersection that nucleates a microcrack from the twin tips (arrow 1).

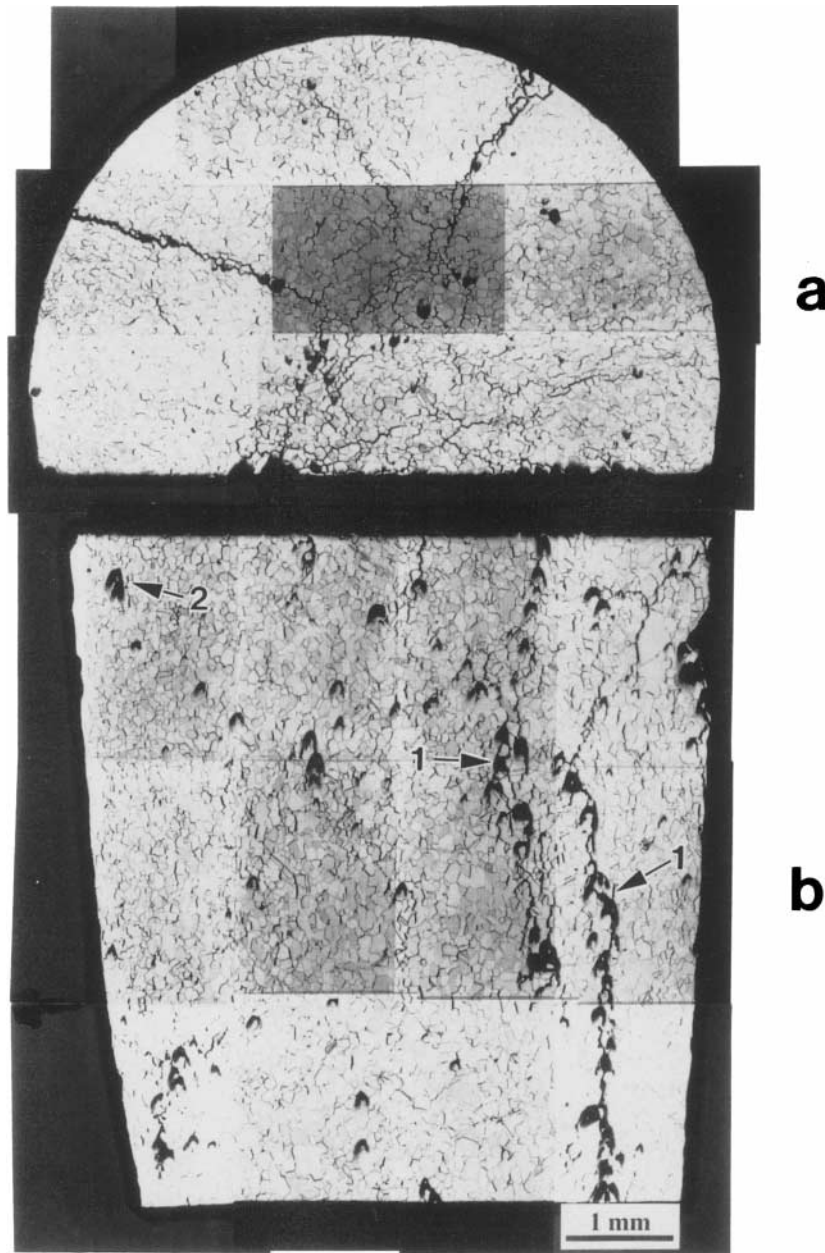
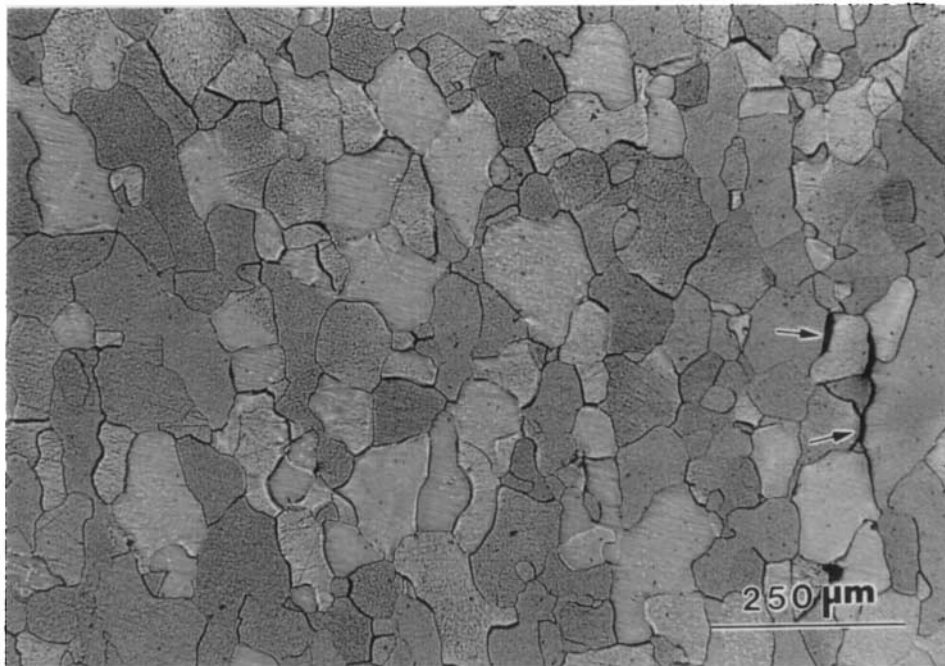


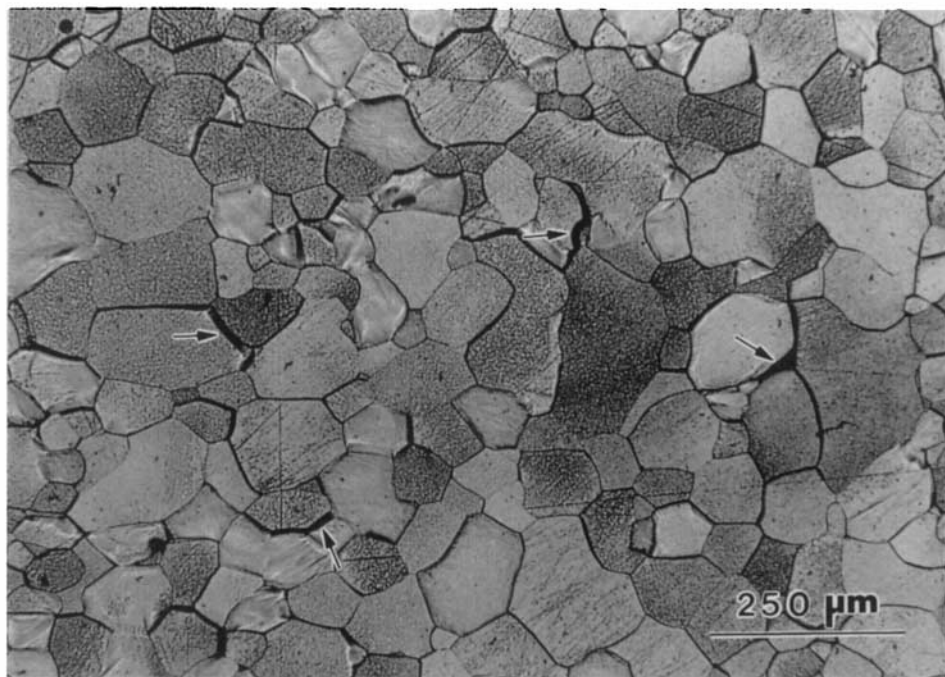
Fig. 4. W annealed at 2600°C, deformed to a strain of 5% ($\dot{\epsilon} = 10^3/s$): (a) cross section and (b) longitudinal section.

Argon and Maloof [25] also observed this in tungsten [011] single crystals and Edmondson [26] in [011] in iron. They concluded that a crack could be formed when the twin intersection line lies in a (001) cleavage plane; in this case the shear due to the crossing twin can be accommodated by nucleation of cleavage cracks. Propagation of these cracks requires further deformation, since the driving tensile stress is exhausted after the crack is initiated. Figure 7(a) also shows a twin crossing the entire grain and connecting the opposite grain boundaries (arrows). At the twin-grain boundary intersections grain-boundary failure occurred. In this case, it is

obvious that the twin initiated microcracking and it is unlikely that both cracks preceded the twin in such a configuration [27]. The micrograph in Fig. 7(b) shows cracks within twinned areas, indicated by 3. These cracks may have been nucleated during twin formation to relieve the tensile stresses within the twin. These cracks were also observed by Subhash *et al.* [8] in (011) textured polycrystalline tungsten. Argon and Maloof [25] concluded that these cracks are initiated at the twin boundaries and can extend over the twinned region due to further deformation.



(a)

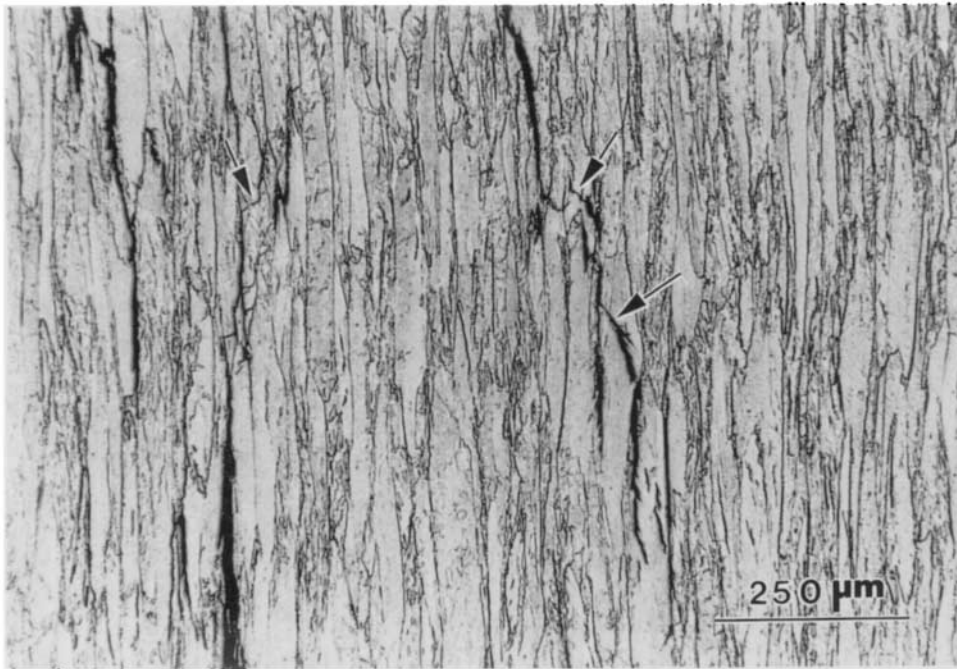


(b)

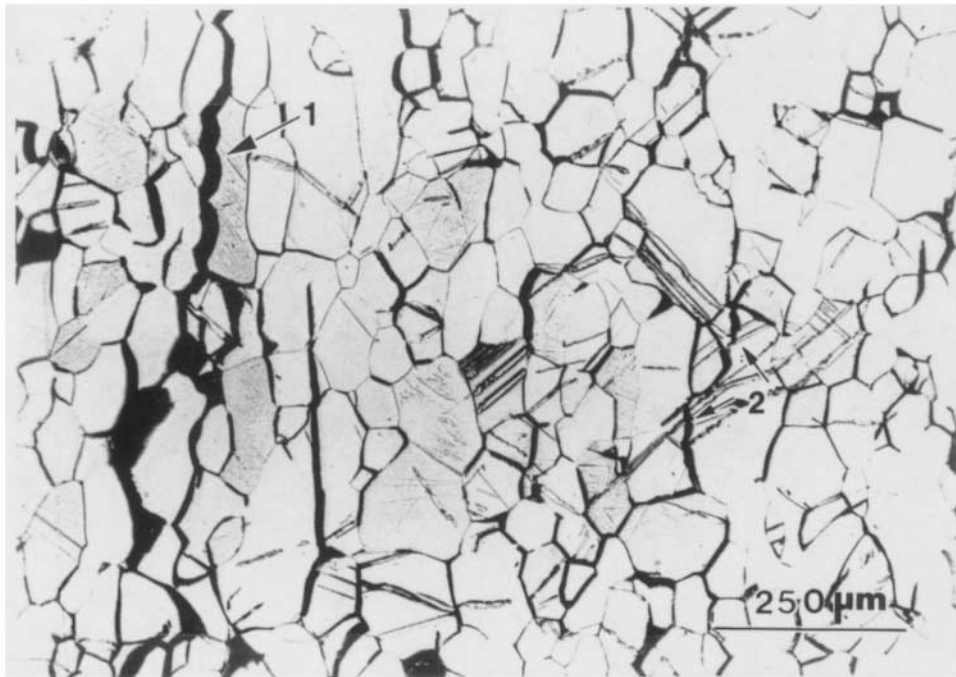
Fig. 5. Annealed W quasi-statically tested to ~25% strain: (a) 1750°C; (b) 2600°C.

The tips of two twins in Fig. 7(b) intersect with two planar transgranular cracks, marked by arrows 4. Subhash *et al.* [8] observed this also in (011) textured tungsten. It supports the conclusion that the

cracks initiated twinning. This is indicated by the difference in contrast of the twinned and untwinned area. Subhash *et al.* [8] and Argon and Maloof [25] proposed that if the twins were formed first, the



(a)

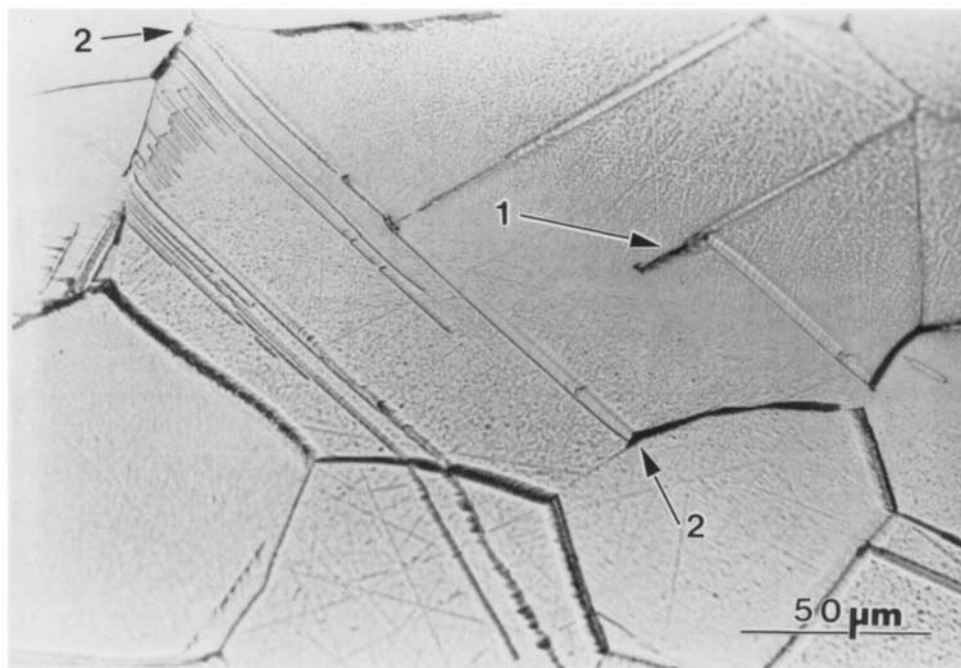


(b)

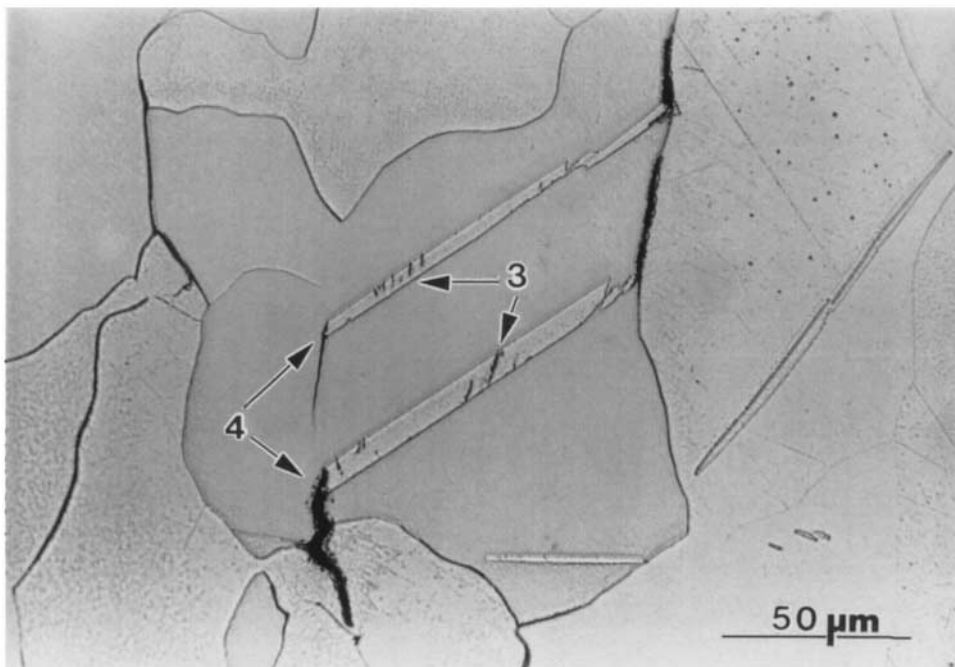
Fig. 6. (a) Longitudinal section of as-received W, deformed to a strain of 9.4% ($\dot{\epsilon} = 3 \times 10^3/s$); (b) longitudinal section of W annealed at 2600°C, deformed to 5.2% ($\dot{\epsilon} = 4 \times 10^3/s$).

cracks would have entered the twins and the contrast across the crack surfaces would be the same. The present result confirms their proposal. The

above observations of twin-transgranular crack interaction are very rare compared to the frequency of grain-boundary cracking not related to twinning.



(a)

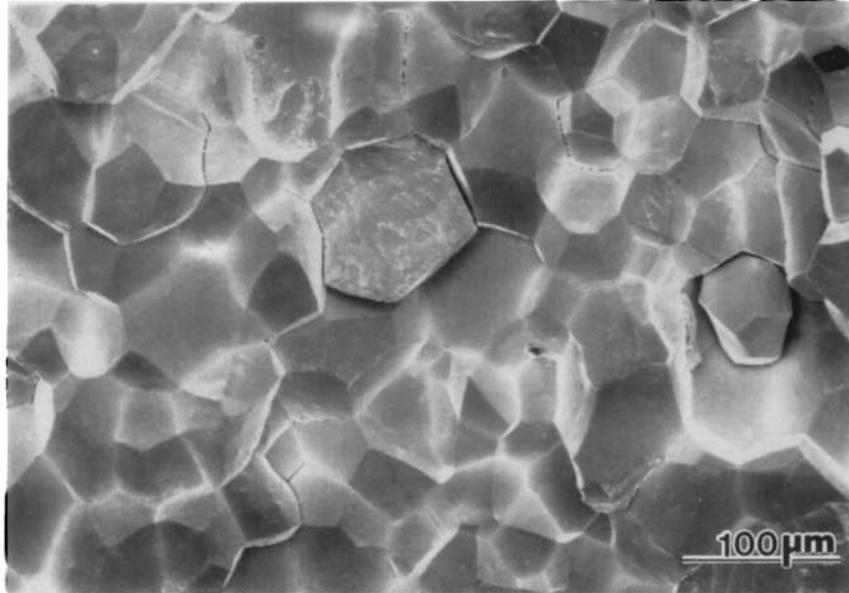


(b)

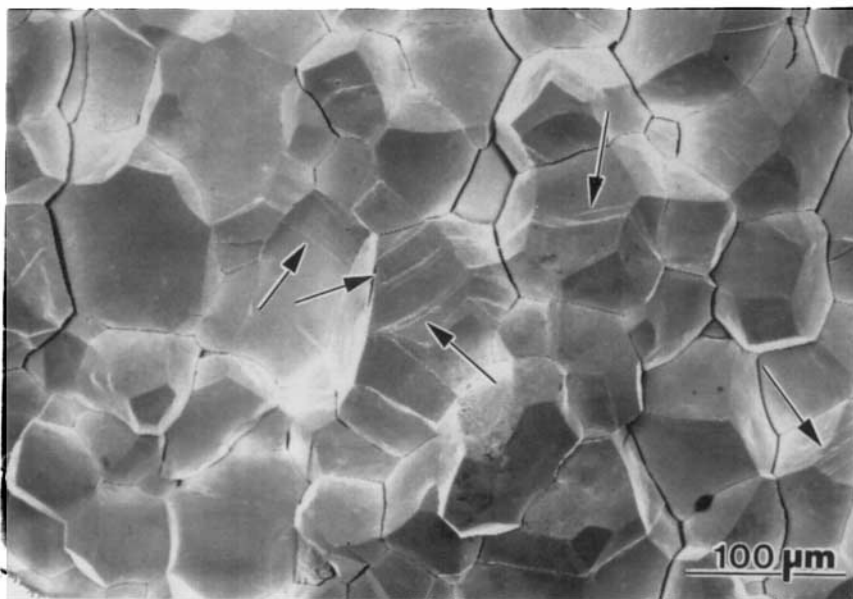
Fig. 7. (a) Crack nucleation at twin intersection (1) and at twin-grain boundary intersection (2); (b) microcracks between twin boundaries (3), and twin nucleation at microcracks (4); W annealed at 2600°C.

It is concluded that twin initiation does not significantly alter damage evolution. Figure 8(a) is a SEM micrograph showing the intergranular fracture surface of a 2600°C specimen deformed to 0.05 strain at a rate of $10^3/s$. The bonds between the adjacent

grains seem to be mainly intact. Figure 8(b) shows the fracture surface of a 2600°C specimen, deformed at a strain rate of $4 \times 10^3/s$. Several twins appear at the grain boundaries (arrows). The twinning incidence is higher than at $10^3/s$, Fig. 8(a).



(a)



(b)

Fig. 8. Fracture surface of 2600°C annealed W, deformed (a) at $10^3/s$ and (b) at $4 \times 10^3/s$.

4. ANALYSIS

4.1. Damage mechanisms

The quantitative analysis presented in the Appendix A clearly shows that (a) damage by cracking increases with increasing strain (at a constant strain rate) and strain rate (at a constant strain) and (b) that the angular distribution of cracks becomes progressively more aligned with the loading axis as the cracks grow or connect. Thus microcracks (which have a random orientation) gradually evolve into axial splitting (which is aligned with the compression axis).

The experimental observations presented in Section 3.4 indicate that there are three competing deformation mechanisms in tungsten: slip, twinning, and grain-boundary decohesion. Due to the strain-rate sensitivity of the flow stress, twinning and grain-boundary decohesion are the favored mechanisms under high-strain-rate conditions. The annealed conditions exhibited grain-boundary decohesion after the onset of plastic flow, due to grain-boundary segregation and associated grain-boundary embrittlement. At high strain rates, the local tensile stresses near the initially present flaws exceeds the grain-boundary cohesive strength at low plastic strains and can lead to the initiation of intergranular brittle fracture immediately after plastic yielding.

Figure 9 shows the stress–strain curves for the material annealed at 1750°C at two strain rates: 10^{-3} and 4×10^3 /s. Also indicated in this figure is a band bound by σ_{ic} and σ_{fc} . These stresses mark the initiation and finish, respectively, of grain-boundary decohesion, and are shown as strain-rate insensitive in Fig. 9. This is a reasonable assumption, because decohesion occurs with a minimum of plastic deformation

and thermal activation should play only a minor role. Figure 9 shows in a very clear fashion that decohesion starts immediately, upon plastic deformation, at 4×10^3 /s, whereas it initiates at $\epsilon_d \sim 0.145$ at 10^{-3} /s. It is possible to develop expressions that describe, in a quantitative fashion, the temperature and strain-rate sensitivities of the various mechanisms; this is done, in a simplified fashion, below.

The grain-boundary decohesion stress decreases with grain size. The effect of increasing the grain size on the grain-boundary decohesion stress is to increase the impurity concentration (P, S, and O) at the grain boundaries. Due to the low solubility for interstitial atoms in tungsten, the total amount of embrittling grain-boundary segregates is expected to be nearly the same in each heat treatment condition. The grain-boundary impurity concentration c_{GB} in mol/unit area then is directly proportional to the grain-boundary area per unit volume. Thus [13]

$$c_{GB} = n \cdot \frac{\pi d}{3} \quad (6)$$

where n is the impurity content in mol/unit volume and d is the grain size. In accordance with Seah [28], a diminution in the grain-boundary decohesion stress $\Delta\sigma_{GB}(c_{GB})$ is caused by an increase in c_{GB} . For simplicity, it is assumed that $\Delta\sigma_{GB}$ increases linearly with c_{GB} . The grain-boundary decohesion stress σ_{GB} can be then described as

$$\sigma_{GB} = \sigma_{ic} - \Delta\sigma_{GB}(c_{GB}) \text{ and } \sigma_{GB} = \sigma_{ic} - kd \quad (7)$$

where σ_{ic} is the decohesion stress of a “clean boundary” and k is a constant. The slope k is given by the total amount of embrittling segregates and their embrittling activity.

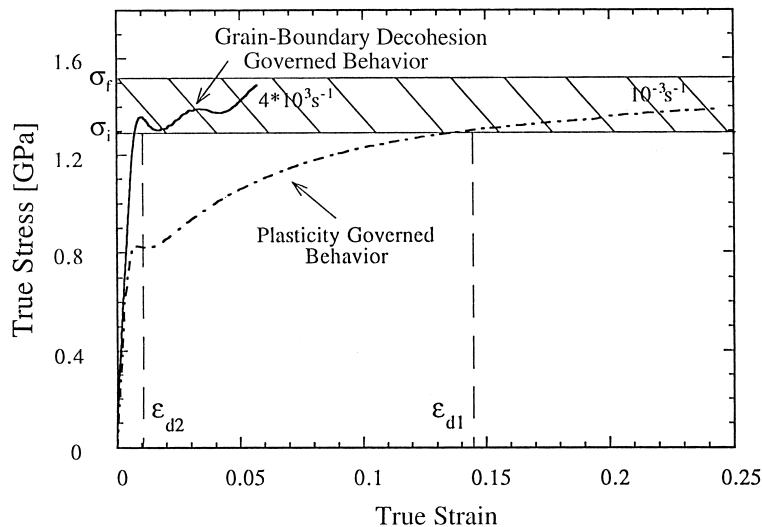


Fig. 9. Schematic description of interactions between plastic deformation and damage at different strain rates by means of stress–strain curves of the 1750°C W: σ_{ic} , initiation of damage; σ_{fc} , catastrophic failure of specimen.

It is known that both the flow and twinning stresses, σ_y and σ_T , can be described by Hall–Petch relationships as a function of grain size [29, 30]:

$$\sigma_y = \sigma_0 + k_S d^{-1/2} \quad (8)$$

$$\sigma_T = \sigma_{0T} + k_T d^{-1/2} \quad (9)$$

where σ_0 and σ_{0T} are the frictional stresses for slip and twinning, respectively, and d is the grain size. The Hall–Petch slope for twinning, k_T , is known to be considerably higher than the one for slip, k_S . For b.c.c. metals, Armstrong and Worthington [31] report $2 < k_T/k_S < 7$. Application of equations (7)–(9) can lead to the mechanism that initiates plastic deformation. The governing mechanism is the one providing the minimum value among σ_{GB} , σ_y , and σ_T .

Two sources for initiation of intergranular cracking within the elastic regime were identified:

1. Initiation of tensile debonding by the sliding displacement of a debonded grain facet (similar to wing cracks in ceramics and rocks).
2. Tensile stress concentrations due to grain-boundary voids.

They are discussed in Sections 4.2 and 4.3, respectively.

4.2. Axial splitting by wing-crack formation

The evidence for a wing-crack formation mechanism in W is shown in Fig. 10(a), taken from the longitudinal section of a 1750°C sample that was deformed to a strain of 0.05 at a rate of $10^3/s$. A number of these events were observed. Two grain-boundary debonds nearly parallel to the loading axis (marked by arrows 3) are linked by a third tilted debond (marked by 1). The step in the plane of the tilted crack (marked by 2) reveals the sliding displacement between the adjacent grains. It is noted that this displacement was initially prevented by the cohesive strength of the grain boundaries that finally separated. Furthermore, it is seen that the displacement of the interfaces of this “sliding crack” created stress concentrations at its tips (marked by 3) producing tension at the points where these tips joined the grain boundaries that failed. It should be emphasized that the mechanism shown in Fig. 10 is a departure from the classical “wing-crack” model of Griffith [32], that was analytically treated by Horii and Nemat-Nasser [22], and Ashby and Hallam [23]. The directions of crack propagation are, in the present case, dictated by grain-boundary orientation and not, as in the former case, by the direction of the maximum principal stress. This will become evident when the Ashby–Hallam equation is applied to the present case by setting the angles of crack propagation [ψ in Fig. 11(a)] as the ones for the grain boundaries, in an ideal arrangement.

Tension is necessary to initiate the vertical cracks aligned with the applied compressive load, according to the Griffith [32] mechanism. Due to the net shear stress, sliding of the two crack surfaces will take place. This leads to local tensile stresses at the tips of the microcrack that will, eventually, nucleate two wing cracks. Horii and Nemat-Nasser [22] and Ashby and Hallam [23] have proposed two-dimensional models for the wing-crack nucleation and propagation. These models describe the influence of the orientation (ψ) of the pre-existing crack and its length $2a$ on the stress intensity factor K_I acting at the tip of a wing crack oriented at an angle θ to the sliding microcrack. The wing cracks are assumed to nucleate once the stress intensity factor at the tip reaches its critical value, K_{Ic} . Figure 11(a) shows schematically how the wing cracks nucleate and grow from an initial sliding crack. Under uniaxial compressive loading, the mode I stress intensity factor K_I acting at the tip of a wing crack can be written as [23]

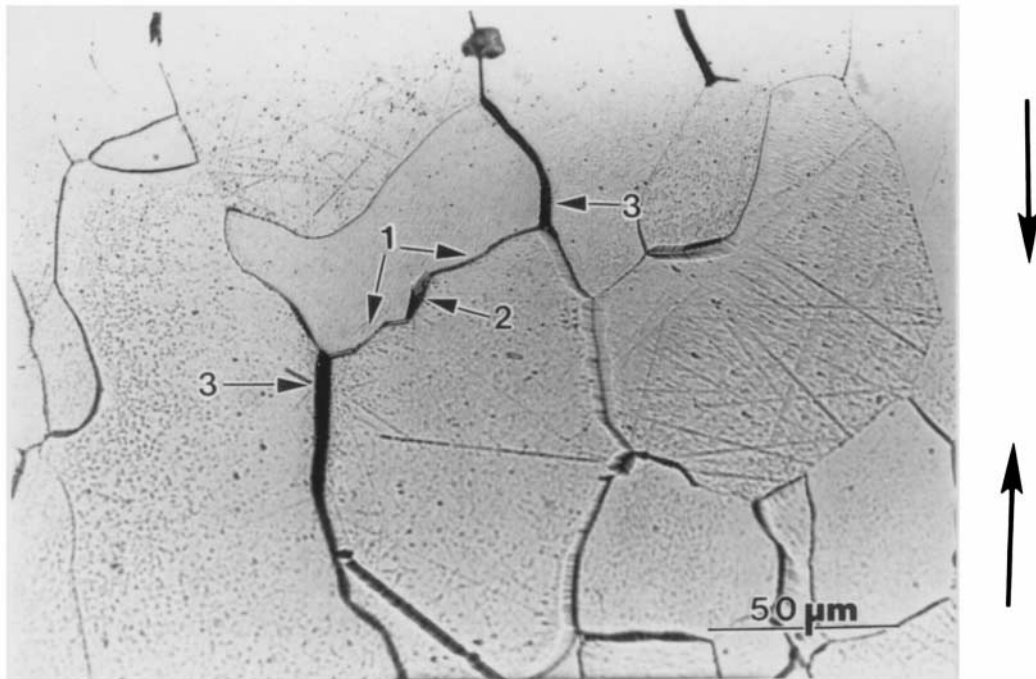
$$K_I = \frac{2}{3} \sigma_1 \sqrt{\pi a} [\eta(1 - \cos 2\psi) - \sin 2\psi] \sin \theta \cos \frac{\theta}{2} \left\{ \frac{\beta L' + (1 + L')^{-1/2}}{(1 + L')^{3/2}} \right\} \quad (10)$$

where σ_1 is the applied stress, η is the coefficient of sliding friction, $2a$ is the length of the pre-existing sliding crack, l is the wing-crack length, $L' = l/a$ is the normalized crack length and the constant $\beta = 0.4$. The frictional force due to the normal force (Coulomb friction) acting on the microcrack surfaces resists sliding and the resolved shear stress due to the external applied stresses acts as the driving force. The stress intensity factor K_I decreases with increasing wing-crack length suggesting stable crack growth with increasing load. This model was developed for studying failure of homogeneous isotropic materials under compressive loading. The corresponding energy release rate, G , can be calculated using

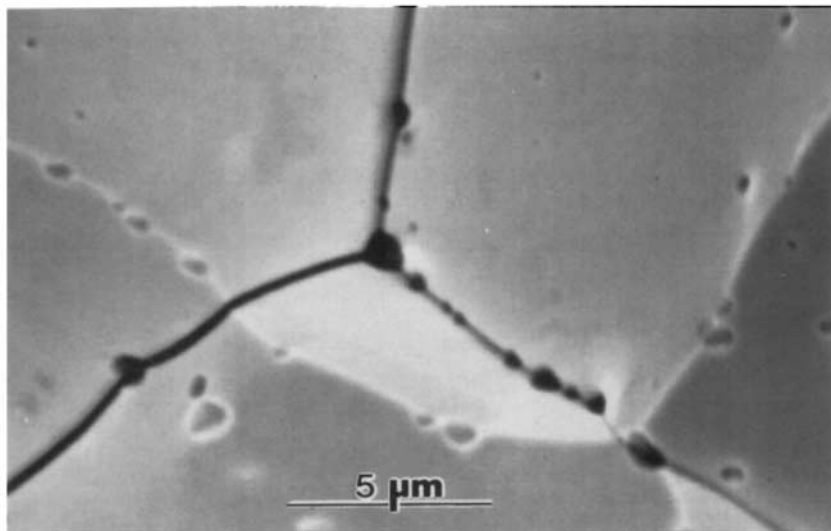
$$G = \frac{K_I^2(1 - \nu^2)}{E} \quad (11)$$

where E and ν are Young’s modulus and Poisson’s ratio of the material, respectively. The energy release rate (G) may be viewed as the cohesive energy for fracture along interfaces.

Tungsten single crystal is known to be elastically isotropic even though its crystal structure has cubic symmetry. Due to the exceptional elastic isotropy of the tungsten single crystal ($A = 1$), the transgranular cracking can be modeled using the wing-crack results, equation (10), and provides a means of estimating the cohesive fracture energy of the grain boundaries. The Young’s modulus (E) and

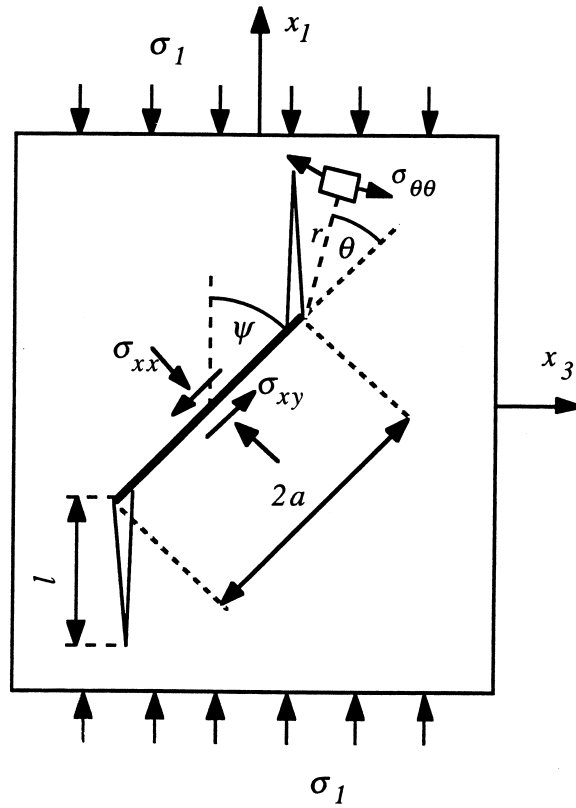


(a)

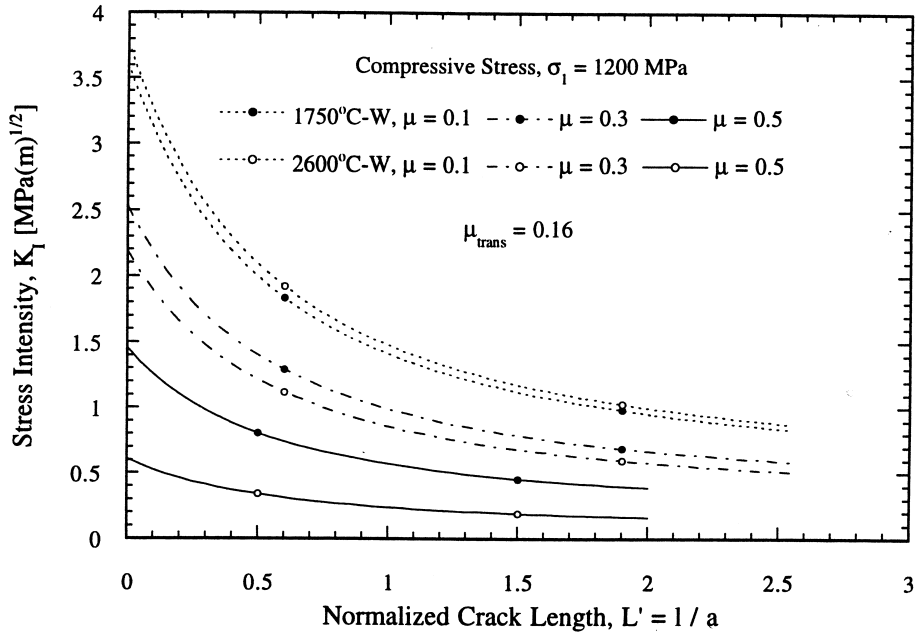


(b)

Fig. 10. (a) Axial “wing cracks” nucleated from shear displacement of the grain boundary inclined to the loading axis; (b) SEM micrograph showing the grain-boundary voids on the fracture surface of a sample annealed at 2600°C.



(a)



(b)

Fig. 11. (a) Schematic of wing-crack formation from the tips of a tilted sliding crack. (b) K_I acting at a wing-crack tip vs normalized crack length L' , for two crack geometries and frictions $\mu = 0.1, 0.3,$ and 0.5 .

Poisson's ratio (ν) of tungsten are 414 GPa and 0.29, respectively.

In the case of annealed tungsten material, the sliding on microcracks [e.g. Fig. 10(a)] presumably takes place during the elastic region of the stress-strain curve. However, it appears that damage by nucleation of wing cracks along the weak grain boundaries does not appear until the stress level reaches $\sigma = 1200$ MPa. The quasi-static stress-strain curve [Figs 2(b)–(d)] exhibits considerable hardening during early stages of deformation typical of annealed materials. Also, note that the material yields around 0.75 GPa and does not develop damage until strains of approximately 0.25 and has hardened to a stress level of 1.2 GPa. In the case of dynamic stress-strain response, it is seen that the material yields at around 1.2 GPa and develops considerable damage even at very small strains of 0.02 (e.g. Fig. 9). Based on these observations, for our analysis using the results from the wing-crack model, we will assume that the wing cracks nucleate when the applied stress level reaches 1200 MPa.

Due to the predominantly intergranular fracture in the 1750 and 2600°C annealed tungsten, the grains need to be mapped in a plane in order to apply the above model. The grain-size estimation (Section 3.1) revealed an equiaxed grain structure for the 2600°C and a 36% grain anisotropy (in the loading direction) for the 1750°C annealed tungsten. In the case of the 2600°C annealed tungsten, the calculated spherical grain diameter d was set as the diameter of the average two-dimensional grain. In the case of the 1750°C annealed material, the crack length $2a$ is determined to be $36.2 \mu\text{m}$ and θ and ψ to be 52.3° . This enables the utilization of the “wing-crack” equations to grain-boundary debonding. In the case of the 2600°C annealed material, the crack length $2a$ is determined to be $50 \mu\text{m}$, and θ and ψ to be 60° . The coefficient of friction η for tungsten is taken to be 0.1, 0.3, and 0.5, which are typical sliding friction coefficients for hard metals [33]. The values for $2a$, ψ , and θ were inserted into equation (10) to calculate the critical mode I stress intensity K_{Ic} at the tip of a representative sliding crack at crack initiation. The critical stress intensity factor K_{Ic} for the annealed material can be calculated from equation (10), using the above values for a , η , ψ , θ , and σ_1 . They are shown in Fig. 11(b). These values are $1.5 \text{ MPa m}^{1/2}$ for the 1750°C and $0.66 \text{ MPa m}^{1/2}$ for the 2600°C annealed material for $L' = 0$ and $\mu = 0.5$. The fracture toughness for the intergranular failure appears to be much smaller than transgranular failure in tungsten, typically $50 \text{ MPa m}^{1/2}$. The cohesive energies of the grain boundaries computed using equation (11) are 5 and 0.96 J/m for the 1750 and 2600°C annealed materials, respectively. The magnitude of cohesive energies supports the concept of increasing embrittlement with annealing temperature discussed in Section 4.1. The grain boundaries in the 2600°C

annealed material are weaker than those in the 1750°C annealed material.

It should be noted that the process of damage accumulation occurs gradually, meaning that a distribution of voids and grain boundaries does exist which require different critical stresses to become activated. The above model assumes that in both materials damage initiates at a constant stress level equal to 1200 MPa as macroscopically indicated by the dynamic stress-strain curves. But it is reasonable to assume that within the 2600°C material the number of debonded grain boundaries or voids is larger than in the 1750°C annealed tungsten and that damage is initiated at a lower stress level. This is confirmed by the observation of more embrittled grain boundaries in the 2600°C annealed material.

4.3. Failure originating from grain-boundary voids

A second mechanism for axial grain-boundary failure under high-strain-rate compression is due to pre-existing grain-boundary voids, acting as stress concentrators. Scanning electron microscopy of the 1750 and 2600°C annealed material shows that pre-existing voids were formed predominantly at these grain-boundary triple points, see Fig. 10(b). These voids are sources for initiation of grain-boundary failure, acting as stress concentrators. Figure 12(a) shows a spherical void schematically. Based on elastic theory, Goodier [34] formulated a solution for the hoop (circumferential) stress acting at the north and south pole of a spherical void in a uniaxial stress field as

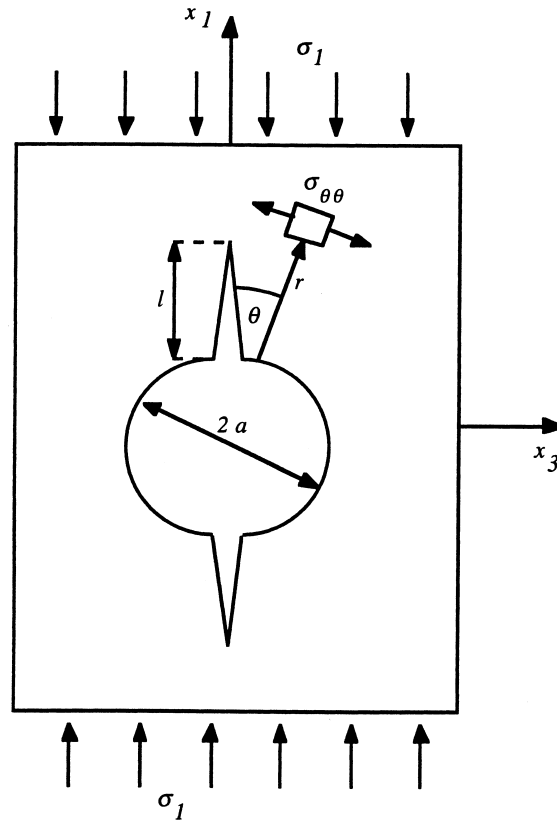
$$\sigma_{\theta\theta}(\theta = 0, \pi; r = a) = -\frac{3(1 + 5\nu)}{2(7 - 5\nu)}\sigma_1 \approx -\frac{1}{2}\sigma_1 \quad (12)$$

where r is the radial coordinate of the void, a is its radius, and ν is Poisson's ratio. Thus, the maximum tensile stress $\sigma_{\theta\theta}$ acts at the poles of the void with respect to the direction of σ . The maximum tensile stress is roughly half of the far-field applied stress for a Poisson's ratio of 0.3 which is a typical value for metals. If tension cracks are initiated they will grow in the loading direction, as indicated in Fig. 12(a).

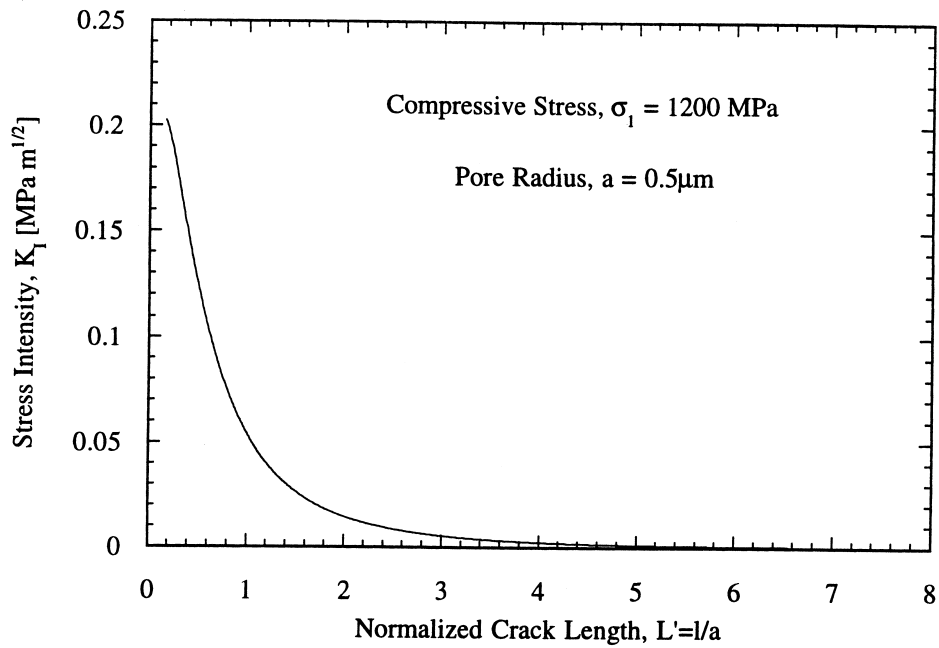
Sammis and Ashby [35] developed an expression for the mode I stress intensity acting at the tip of a crack of length l emanating from the poles of a void of radius a situated in a field of uniaxial compression [Fig. 12(a)]:

$$K_I = -L'^{1/2} \frac{0.62}{(1 + L')^{4.1}} \sigma_1 \sqrt{\pi a} \quad (13)$$

where L is the normalized crack length and equal to l/a . From Fig. 10(b) the radius a of a representative grain-boundary void within the material annealed at 2600°C is estimated to be $0.5 \mu\text{m}$. The stress intensity acting at the tips of initiated cracks can be calculated by means of equation (13). Figure 12(b) shows the stress intensity caused by a void of



(a)



(b)

Fig. 12. (a) Schematic of axial crack initiation by spherical void; (b) stress intensity acting at the tips of an axial crack, nucleated by a grain-boundary void as a function of the normalized crack length L' .

radius $a = 0.5 \mu\text{m}$ as a function of the normalized crack length L . The applied compressive stress is taken as $\sigma_1 = 1200 \text{ MPa}$, close to the macroscopic yield strength under high-strain-rate conditions, see Figs 2(b) and (c). The stress intensity at crack initiation is much lower than that achieved due to the displacement of a sliding crack shown in Fig. 12(b). Furthermore, K_I decreases faster for increasing crack length when caused by a void than by a tilted sliding crack. It appears that a void of radius $0.5 \mu\text{m}$ is not capable of causing the complete debond of the affected grain-boundary facet. The SEM micrograph in Fig. 10(b) shows numerous voids of similar radius aligned at grain-boundary triple points. Overlapping of the stress fields can cause an increase in stress intensity that, eventually, can cause debonding of the affected grain boundary. Therefore, the distribution of these grain-boundary voids seems to be very important. Randomly distributed, their effect on grain-boundary failure does not appear to be critical; however, agglomerations of voids can be seen as serious sources for intergranular fracture.

4.4. Damage evolution

The two fracture mechanisms discussed above deal with the initiation of damage. The cracks are treated as a dilute distribution, with no interaction between them. Figure 4 shows that cracks interact when a particular amount of damage is accumulated. Individual grain-boundary debonds coalesce to mainly axially oriented macrocracks (Fig. 4). The growth behavior of cracks is influenced by their interactions. Figure 6(b) shows a longitudinal section of a 2600°C sample deformed to a strain of 0.052 at a rate of $4 \times 10^3/\text{s}$. An axial macrocrack is indicated by arrow 1. Note that the grain shape is not randomly distributed. The macrocrack travels along boundaries of elongated grains. A possible mode for the macrocrack formation is that several aligned cracks grow and coalesce by grain-boundary debonding between them. An initially discrete axial row of microcracks becomes gradually more continuous and divides the specimen into parallel columns. Additional axially linked cracks will cause a loss in strength of the specimen at a remaining load, yielding crack propagation to catastrophic failure [23]. This mechanism may result in the low amount of grain-boundary fracture in the vicinity of axial macrocracks, which is frequently observed by metallography [Figs 4 and 6(b)].

5. SUMMARY AND CONCLUSIONS

The results of the present investigation are summarized below:

1. The failure mode in all heat-treated material is predominantly of intergranular character. The as-received tungsten exhibits a larger fraction of

transgranular damage that is governed by cracks tilted from the loading and texture orientation.

2. The flow stress (by slip) has a strain-rate sensitivity that is well described by the MTS constitutive equation; grain-boundary decohesion seems to have a much lower strain-rate sensitivity.
3. Slip, twinning, and grain-boundary cracking are competing deformation mechanisms, the former being favored under quasi-static and the latter two under high-strain-rate conditions. As a consequence, the material undergoes a ductile-to-brittle transition as the strain rate is increased from 10^{-3} to $10^3/\text{s}$. This is seen to be due to the strong strain-rate sensitivity of the flow stress exhibited by tungsten typical of b.c.c. metals. At high strain rates the higher values of axial stress cause sliding of the microflaws, leading to initiation of intergranular fracture resulting in axial splitting at small strain levels. The total density of grain-boundary debonds at constant strain and strain rate increases with heat treatment temperature. This is due to a corresponding increase in concentration of embrittling grain-boundary segregates.
4. Failure in all tested material at high strain rates is seen to be governed by propagation of axial cracks which link the end surfaces of the cylindrical specimens. In particular, at a strain rate of $10^3/\text{s}$ the area close to these major cracks seems to be free of further damage.
5. Optical microscopy reveals that twins were only formed in the heat-treated material and only at strain rates of 10^3 and $4 \times 10^3/\text{s}$. The density of twins increases with strain rate and with strain. Twins are always related to grain-boundary debonds. Twin-twin intersections often yield transgranular microcracks. The latter fracture is also observed within twinned areas. It is shown that twinning is seldom related to cracks that are prone to yield catastrophic failure of the respective sample. Thus, twinning does not play a major role in damage evolution. SEM fracture surface observations show that no slip bands intersect with debonded grain boundaries that are related to major cracks. Fracture initiation at high strain rates therefore is seen to be initiated by failure of weak grain boundaries or stress concentrations caused by voids located at the grain boundaries.
6. Two mechanisms were observed for damage initiation: (a) sliding cracks from debonded grain boundaries which nucleate wing cracks close to the loading direction; (b) microcrack nucleation due to stress concentrations created by pre-existing grain-boundary voids which is frequently observed in the material heat treated at 2600°C . The predictions of both damage mechanisms support the idea of increasing grain-boundary brittleness with higher heat treatment temperatures accompanied by a decrease in grain-bound-

ary fracture toughness. Application of the wing-crack mechanism enables the estimation of the cohesive energy of the grain boundaries.

Acknowledgements—This research was partially supported by the U.S. Army Research Office under the URI Program on Ultradynamic Performance of Materials (Contract: ARO DAAL 03-92-G-0108) and the U.S. Army Research Laboratory through W. Bruchley. This work is part of an exchange program coordinated at the University of Karlsruhe (TH) by O. Vöhringer. Appreciation is extended to K. S. Vecchio, D. Harach, and A. Rohatgi for performing the quasi-static compression tests, to A. J. Strutt for help in metallography, to J. Hodowany and D. Owen for performing the high-strain-rate compression tests, and to H.-C. B. Chen, Y.-J. Chen, and J. Shih for helpful discussions. The 1750°C heat treatments were carried out at Sandia National Laboratories through the kind help of A. Romig Jr and M. Karnowsky. The constructive criticism by the referee is greatly appreciated.

REFERENCES

1. Penrice, T. W., *Metals Handbook*, Vol. 7, 9th edn. Metals Park, Ohio, 1984, p. 688.
2. Magness, L. S., *Mech. Mater.*, 1994, **17**, 147.
3. Srikanth, V. and Upadhayaya, G., *Refractory Hard Metals*, 1986, **5**, 49.
4. Chilton, A. C. and Wronsky, A. S., *J. less-common Metals*, 1969, **17**, 447.
5. Lassila, D. H. and Gray, G. T. III, *J. Physique IV*, 1994, **4**, C8-349.
6. Ravichandran, G., *Mater. Manufacturing Processes*, 1994, **9**, 1031.
7. Subhash, G., Lee, Y. J. and Ravichandran, G., *Acta metall.*, 1994, **42**, 319.
8. Subhash, G., Lee, Y. J. and Ravichandran, G., *Acta metall.*, 1994, **42**, 331.
9. Chiem, C. Y. and Shyan, L. W., *Mater. Sci. Engng*, 1994, **A187**, 43.
10. Follansbee, P. S., *Metals Handbook*, Vol. 8, 9th edn. Metals Park, Ohio, 1984, p. 198.
11. Chen, W., Subhash, G. and Ravichandran, G., *DYMAT J.*, 1994, **1**, 193.
12. Nemat-Nasser, S., Isaacs, J. B. and Starrett, J. E., *Proc. R. Soc. Lond. A*, 1991, **435**, 371.
13. DeHoff, R. T. and Rhines, F. N., *Quantitative Microscopy*. McGraw-Hill, New York, 1968.
14. Zerilli, F. J. and Armstrong, R. W., *J. appl. Phys.*, 1986, **61**, 1816.
15. Meyers, M. A., Chen, Y.-J., Marquis, F. D. S. and Kim, D. S., *Metall. Trans. A*, 1995, **26A**, 2493.
16. Andrade, U., Meyers, M. A., Vecchio, K. S. and Chokshi, A. H., *Acta metall.*, 1994, **42**, 3183.
17. Zurek, A. K., Follansbee, P. S. and Kapoor, D., in *High Strain Rate Behavior of Refractory Metals and Alloys*, ed. E. Chen and A. Crowson. TMS, 1992, p. 179.
18. Kocks, U. F., Argon, A. S. and Ashby, M. F., *Prog. Mater. Sci.*, 1975, **19**, 1.
19. Follansbee, P. S., in *Metallurgical Applications of Shock-Wave and High-Strain Rate Phenomena*, ed. L. E. Murr, K. P. Staudhammer and M. A. Meyers. Marcel Dekker, New York, 1986, p. 451.
20. Follansbee, P. S. and Kocks, U. F., *Acta metall.*, 1988, **36**, 81.
21. Chen, S. R. and Gray, G. T., *2nd International Conference on Tungsten and Refractory Metals*. Metals Powder Industries Federation, Princeton, 1995, p. 489.
22. Hori, H. and Nemat-Nasser, S., *J. Geophys. Res.*, 1985, **90**, 3105.
23. Ashby, M. F. and Hallam, S. D., *Acta metall.*, 1986, **34**, 497.
24. Bilello, J. C., *Trans. metall. Soc. A.I.M.E.*, 1968, **242**, 703.
25. Argon, A. S. and Maloof, S. R., *Acta metall.*, 1966, **14**, 1463.
26. Edmondson, B., *Proc. R. Soc. Lond. A*, 1961, **264**, 176.
27. Reid, C. N., *Metall. Trans. A*, 1981, **12A**, 371.
28. Seah, M. P., *Acta metall.*, 1980, **28**, 955.
29. Löhe, D. and Vöhringer, O., *Z. Metallk.*, 1986, **77**, 557.
30. Hull, D., *Acta metall.*, 1961, **9**, 191.
31. Armstrong, R. W. and Worthington, P. J., in *Metallurgical Effects at High Strain Rates*, ed. R. W. Rohde, B. M. Butcher, J. Holland and C. Karnes. Plenum Press, New York, 1973, p. 401.
32. Griffith, A. A., *Proc. 1st Int. Congr. Appl. Mech.*, Delft, 1924, p. 55.
33. Bowden, F. P. and Tabor, D., *Friction and Lubrication*. Clarendon Press, Oxford, 1956.
34. Goodier, J. N., *J. appl. Mech.*, 1933, **1**, 39.
35. Sammis, C. G. and Ashby, M. F., *Acta metall.*, 1986, **34**, 511.
36. Dümmer, T., *Diplomarbeit*, Universität Karlsruhe (TH), Institut für Werkstoffkunde I, 1996.

APPENDIX A

Quantitative damage analysis

Concerning the damage quantification, only the intergranular grain-boundary failure was taken into account, since the amount of transgranular damage was negligible at all strain rates for the annealed conditions. Since the as-received W exhibited a large transgranular contribution to the accumulated damage, it will not be presented here. Damage was initiated by single grain-boundary debondings of the length of one grain-boundary facet or less and propagated by coalescing of grain-boundary debondings. As characteristic feature of damage, the total number of complete debonded grain-boundary facets and those that were not separated over the whole length of the facet were recorded by counting from the micrographs. The crack length is normalized to the length of a grain-boundary facet. The following classification was used: $L < 3$; $3 < L < 7$; $L > 7$. This is an arbitrary classification, but it enables "tracking down" the fracture events (both in orientation and in density) as they develop throughout the material. The microcracks ($L \sim 1-3$) are the initiating events and are the result of individual grain-boundary debonding. They coalesce and grow, and they gradually lead to the catastrophic failure of the specimen.

Furthermore, the angle of each of those debondings with the loading axis was estimated by superimposing a transparent sheet marked with lines at angles of 0, 20, 40, 60, 80 and 90 deg on the images. The orientations falling within these ranges were estimated.

The damage was not seen to be randomly distributed and the size distribution of cracks appeared to be different at different sites on the polished surfaces. Therefore, it was decided not to use an intersect method, but simply to count the debondings over the entire photographed area of the specimen sections.

The data is presented in two types of plots for each condition:

1. Distribution of intergranular cracks (in number per unit area) vs the crack length categories in terms of L , the apparent number of debonded grain-boundary facets of which the cracks consist; L is referred to as the fractional crack length (equal to the ratio of crack length, L , to single facet length, F). Hence $L < 1$ represents an incompletely debonded grain-boundary

facet; $L = 1$ a debonded facet. The following ranges were established: $0 < L < 3$; $3 < L < 7$; and $L < 7$.

2. Distribution of intergranular cracks (in number per unit area) vs the angle from the loading axis for each observed crack length category. In case of cracks consisting of linked grain-boundary debonds, $L > 1$, the angle of the entire crack is given.

Figures A1–A4 show the results for the longitudinal sections of the 1750 and 2600°C annealed tungsten, respectively. The results for the 2800°C tungsten are presented elsewhere [36]. Figure A1 compares the results for 10^{-3} and $10^3/s$ (1750°C annealed condition). It should be noted that the damage at $10^3/s$ is considerably higher, especially for larger macrocracks, in spite of the lower total strain (0.038 vs 0.26). The smaller microcracks show a much more random orientation; as they connect and their length increases ($L > 7$), the orientation along the loading axis is

strongly favored. As the strain rate is increased from 10^3 to $4 \times 10^3/s$ (Fig. A2) for the same total strain (~ 0.05), the amount of damage increases. This is consistent with Fig. A1. The same trend is observed for the material annealed at 2600°C. Damage is somewhat lower at $10^3/s$ than at $10^{-3}/s$ (Fig. A3) however, it should be noticed that the plastic strain is tentimes higher at 10^{-3} (~ 0.26) than at $10^3/s$ (~ 0.025). Also note that with an increase in strain rate from 10^3 to $4 \times 10^3/s$, the extent of damage increases, for a fixed strain (~ 0.05), Fig. A4.

These results show in a most clear fashion that (a) the damage by cracking increases with increasing strain and strain rate, and (b) that the angular distribution of cracks becomes progressively more aligned with the loading axis as the cracks grow or connect.

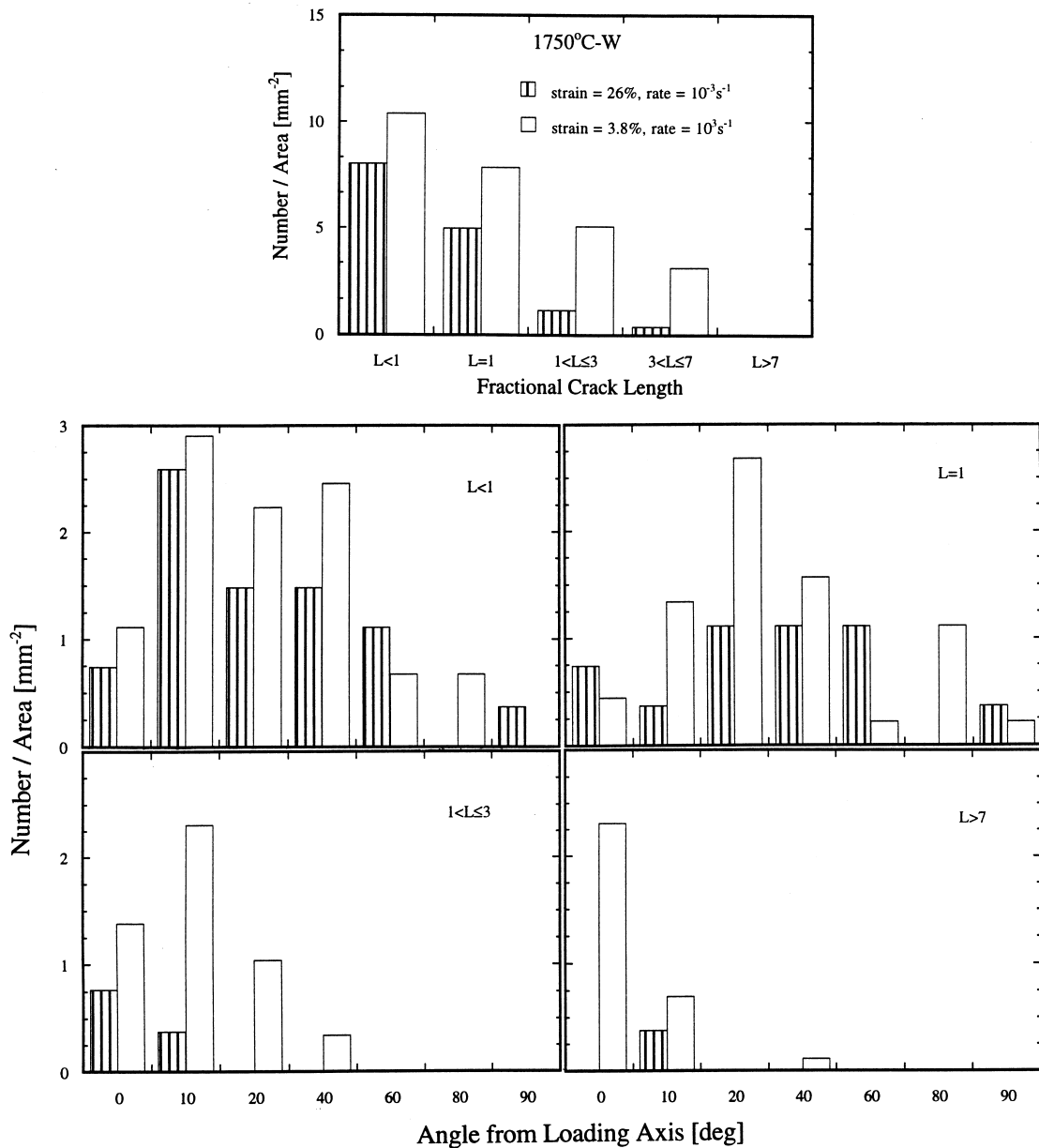


Fig. A1. Damage in W annealed at 1750°C; showing a profound increase in damage, for increasing strain rates from 10^{-3} to $10^3/s$ (note great difference in strains: 26% at $10^{-3}s^{-1}$ and 3% at 10^3s^{-1}).

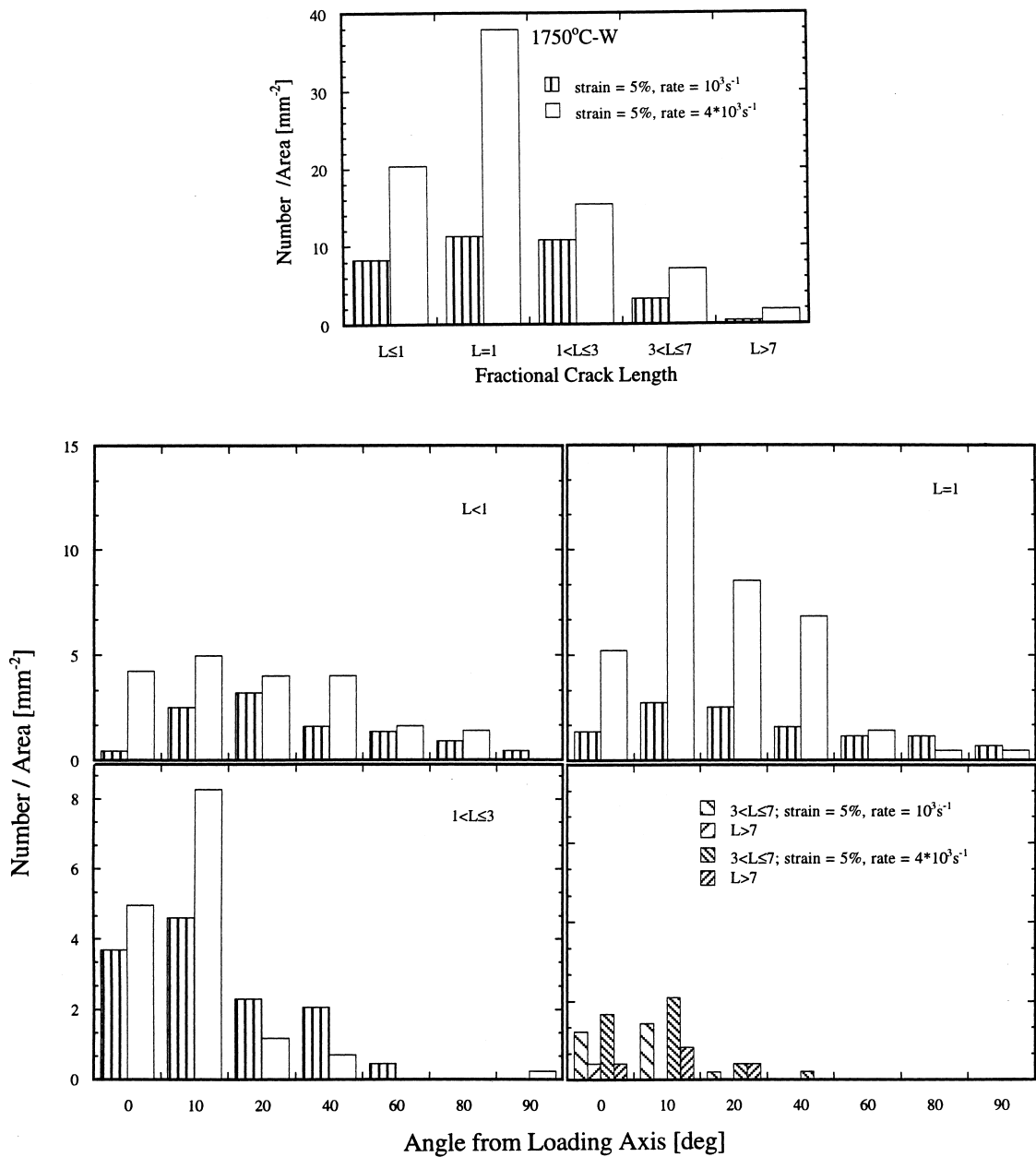


Fig. A2. Damage in W annealed at 1750°C; showing increase in damage, for increasing strain rates from 10^3 to $4 \times 10^3/\text{s}$ at constant strains.

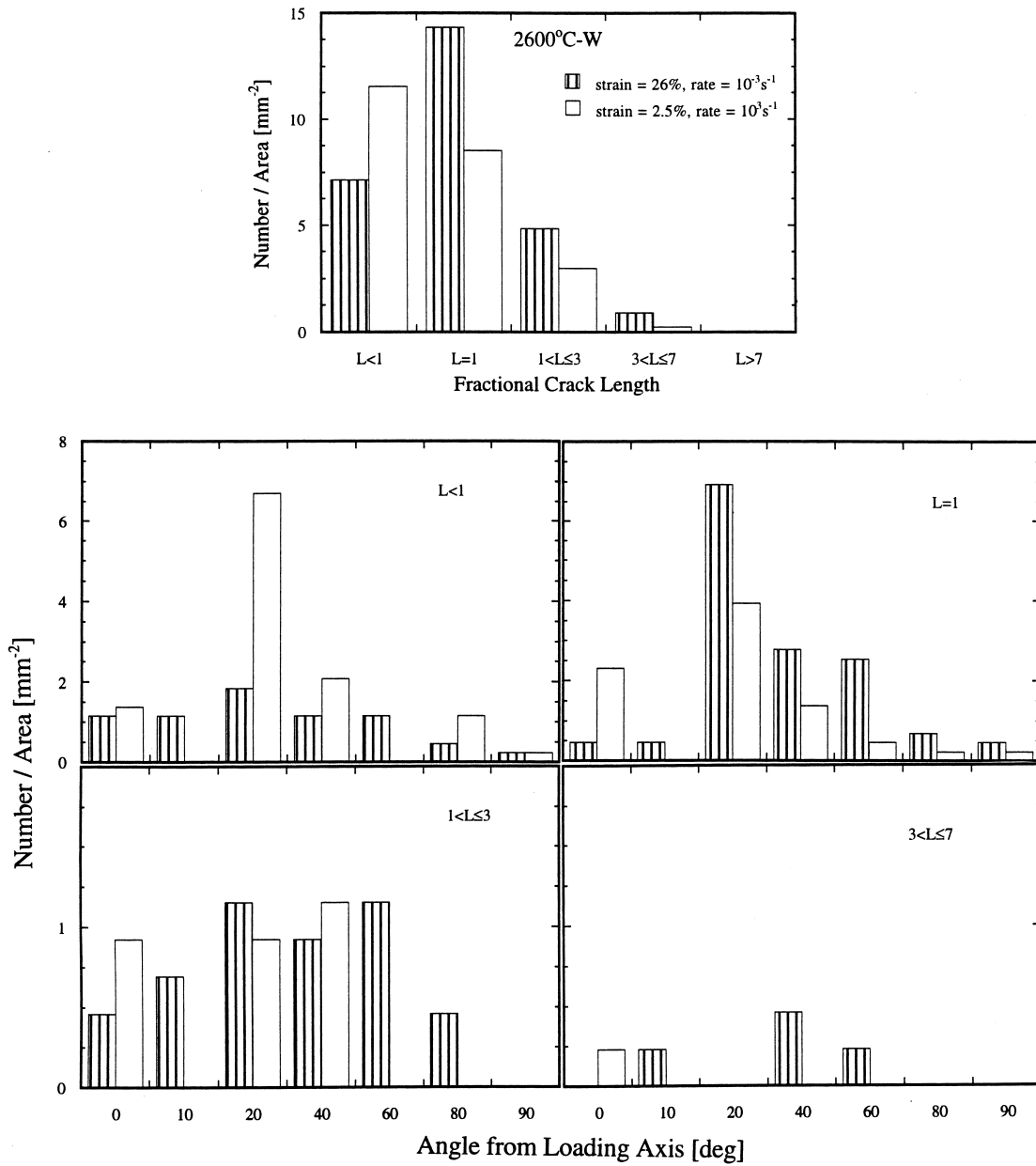


Fig. A3. Damage in W annealed at 2600°C; showing a profound increase in damage, for increasing strain rates from 10⁻³ to 10³/s (note great difference in strains: 26% at 10⁻³s⁻¹ and 25% at 10³s⁻¹).

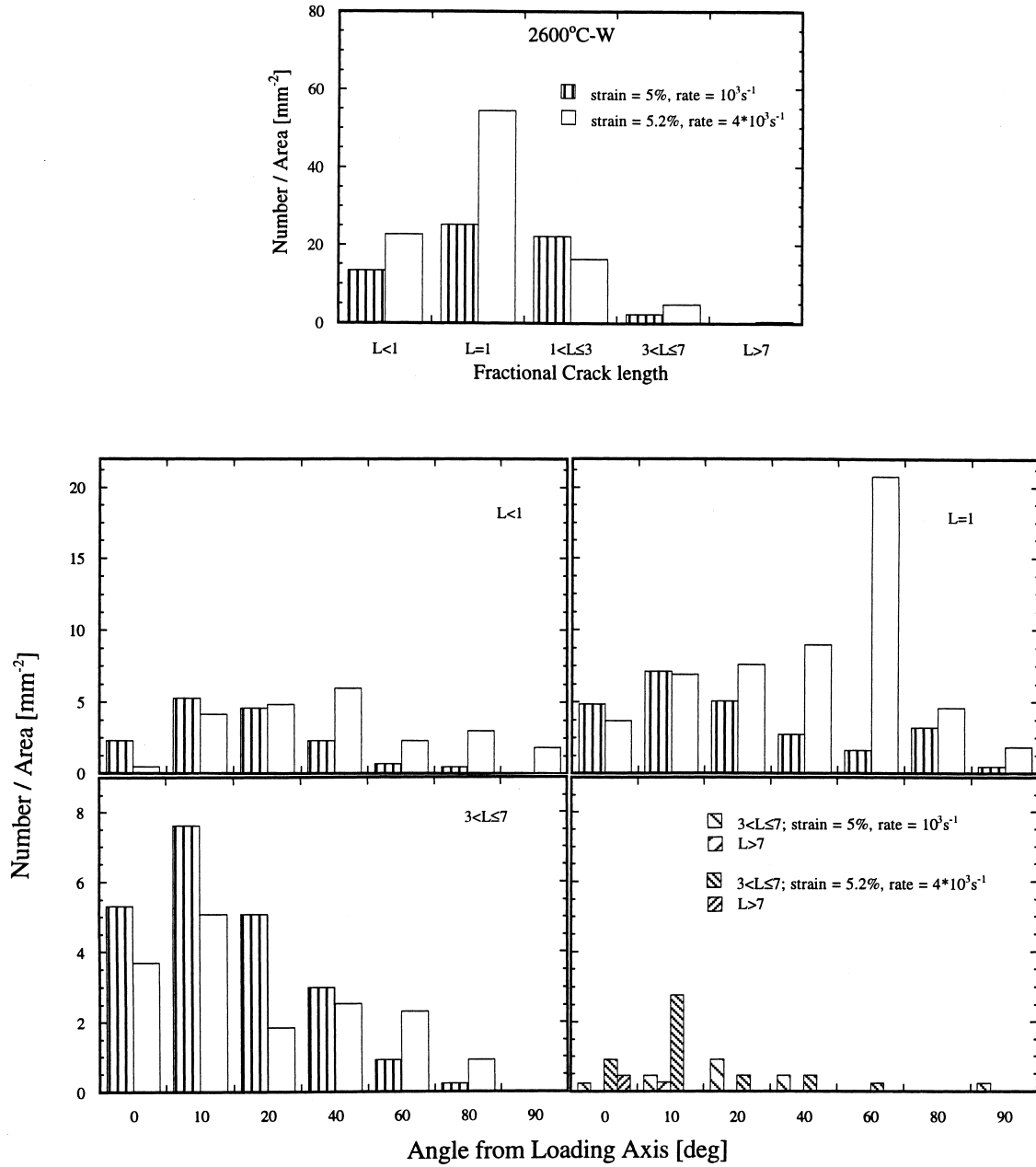


Fig. A4. Damage in W annealed at 2600°C; showing increase in damage, for increasing strain rates from 10³ to 4 × 10³/s at constant strains.